Published for SISSA by Springer

Received: May 29, 2025
Revised: August 2, 2025
Accepted: September 8, 2025
Published: October 10, 2025

Dirac Scoto inverse-seesaw from A_4 flavor symmetry

Ranjeet Kumar,[a] **Newton Nath**,[b] **Rahul Srivastava**[a] **and Sushant Yadav**[a]

[a] *Department of Physics, Indian Institute of Science Education and Research - Bhopal, Bhopal Bypass Road, Bhauri, Bhopal, India*

[b] *Department of Physics, Indian Institute of Technology (BHU), Varanasi 221005, India*

E-mail: ranjeet20@iiserb.ac.in, nnath.phy@iitbhu.ac.in, rahul@iiserb.ac.in, sushant20@iiserb.ac.in

Abstract: We present a Dirac scotogenic-like one loop radiative model where the stability of dark matter is intricately linked to the breaking of A_4 flavor symmetry. This breaking induces a $\mathcal{Z}_2$ dark symmetry, stabilizing the dark matter candidate. The breaking of $A_4 \to \mathcal{Z}_2$ leads to cutting the loop and facilitating a "scoto inverse-seesaw" mass mechanism responsible for neutrino mass generation. This elucidates the explicit explanation of two mass-squared differences, $\Delta m^2_{\rm atm}$ and $\Delta m^2_{\rm sol}$ observed in neutrino oscillations. Our model accounts for normal and inverted ordering of neutrino masses, revealing sharp correlations between $\sum m_i$ and $\langle m_\beta \rangle$. It also shows strong compatibility with current data in the $\delta_{\rm CP}$–θ_{23} plane. Moreover, stringent constraints on scalar masses narrow down the viable dark matter mass regions, accommodating $\mathrm{SU}(2)_L$ singlet and doublet scalar dark matter as well as fermionic dark matter. Additionally, our model presents a viable avenue for addressing lepton flavor violating decays while remaining consistent with current experimental constraints.

Keywords: Models for Dark Matter, Neutrino Mixing, Particle Nature of Dark Matter, Lepton Flavour Violation (charged)

ArXiv ePrint: 2505.01407

https://doi.org/10.1007/JHEP10(2025)088

Contents

1 Introduction

The discovery of non-zero neutrino masses and mixing in neutrino oscillation experiments [1, 2], along with compelling evidence that approximately 85% of the Universe's total matter exists as dark matter (DM) [3], has drawn significant interest from particle physicists. These observations point to clear shortcomings of the otherwise successful Standard Model (SM), which cannot account for neutrino masses or the nature of DM. Additionally, the question of whether neutrinos are Dirac or Majorana particles in nature has remained a long-standing puzzle, continuing to attract considerable attention in the field. These interesting aspects have driven efforts to explore physics beyond the Standard Model (BSM) for a deeper understanding of such phenomena. From a theoretical viewpoint, various models have been proposed in the literature to explain the tiny masses of neutrinos and the origin of DM within a unified framework. One widely acclaimed model is the "scotogenic" mechanism [4], a minimal extension of the SM that links DM stability to neutrino mass generation and treats neutrinos as Majorana particles. Although these models offer insight into the smallness of neutrino masses and DM stability, they are often criticized for their difficulty in explaining

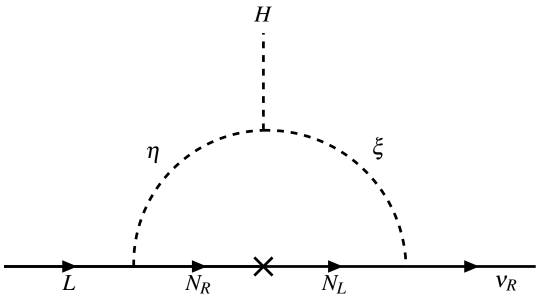

Figure 1. Dirac scotogenic model for neutrino mass generation.

the flavor structure of the leptonic sector, and the two different mass scales observed in neutrino oscillation experiments [5–7] namely, atmospheric, Δm^2_{atm}, and the solar, Δm^2_{sol}. The scoto-seesaw model, recently addressed in [8], is one possible way to explain the origin of the two different mass scales of neutrino oscillation in addition to DM. Within this framework, Δm^2_{atm} arises from scoto-loop, while Δm^2_{sol} appears at the tree level seesaw [8–17]. However, scoto-seesaw models do not shed any light on the mixing and flavor structure of the leptonic sector like other neutrino mass mechanisms.

Experimental evidence for the Majorana nature of neutrinos remains inconclusive, as indicated by the results from searches for neutrinoless double beta decay [18]. This leaves open the possibility that neutrinos may instead be Dirac particles, thereby motivating further investigation into their Dirac nature. While the canonical scotogenic model [4] was originally formulated for Majorana neutrinos, the scotogenic framework is sufficiently general to accommodate Dirac neutrinos as well [19, 20]. Indeed, in recent years, several attempts have been made to explore Dirac scotogenic models, as proposed in [21–25]. This model extends the SM by incorporating radiative neutrino mass generation, while ensuring that neutrinos remain Dirac particles.

To address the challenges related to the origin of neutrino masses, their flavor structure, the presence of two distinct mass scales, and the stability of DM, a recent approach based on flavor symmetries has been developed [26–28]. Within this framework, it has been demonstrated that employing the A_4 flavor symmetry [29–31] allows for predictive solutions to the leptonic flavor structure. In addition, the spontaneous breaking of A_4 to its subgroup $\mathcal{Z}_2$ [32–34] ensures DM stability while also leading to the scoto-seesaw mass mechanism. Ref. [26], explore the Majorana scotogenic loop, whereas ref. [27] investigates the Dirac scotogenic loop. Additionally, the authors of [26] emphasize that the mass of DM is tightly constrained by the breaking of A_4 symmetry. They further provide conclusive evidence for the scalar DM scenario by ruling out the possibility of fermionic DM.

In this work, we propose a framework that explains the Dirac nature of neutrinos within the leptonic flavor structure while simultaneously addressing both scalar and fermionic DM scenarios. Overall, our flavor-symmetric approach provides a highly predictive framework for both neutrino sector phenomenology and DM studies, offering compelling theoretical insights into BSM physics. To serve our purpose, we employ A_4 flavor symmetry on a Dirac scotogenic-like radiative loop as shown in figure 1. The spontaneous symmetry breaking

(SSB) of A_4 to its $\mathcal{Z}_2$ subgroup stabilizes the DM candidate. This breaking also leads to the cutting of the loop, inducing a hybrid "scoto inverse-seesaw" mass mechanism. Note that the inverse-seesaw mass mechanism proposed in [35] requires a small mass parameter, usually called μ-term. This naturally emerges in our formalism due to the presence of an SU$(2)_L$ singlet scalar acquiring a vacuum expectation value (VEV), which can be very small. Recently, authors of [36] have addressed this mechanism for both Majorana and Dirac neutrinos. In our formalism, the Dirac neutrino masses are generated at the tree level via the inverse-seesaw mechanism and at the loop level through the scoto-loop.

Here, we also consider an accidental U$(1)_{B-L}$ symmetry, inherently present in the SM, and its breaking into a $\mathcal{Z}_3$ subgroup to prevent tree-level couplings before SSB and to forbid the Majorana neutrino mass term. The chiral anomaly-free $B-L$ symmetry requires the $(-4,-4,5)$ charge assignment for the right-handed neutrinos ν_{R_i} [37–39]. Unlike the Majorana version [26], our model features both normal ordering (NO) and inverted ordering (IO) of neutrino masses. Furthermore, the A_4 symmetric approach imposes an upper bound on the scalar masses based on the two mass-squared differences of neutrino, thereby constraining the allowed parameter space for DM candidates. Also, we study the different charged lepton flavor violation (CLFV) processes and check their viability under different current and future proposed experiments.

This paper is organized as follows. In section 2, we outline the model setup based on A_4 flavor symmetry and discuss the scalar mass spectrum as well as the neutrino sector. We discuss the emergence of the inverse-seesaw mechanism at tree level and scoto-loop due to the breaking of A_4 symmetry. In section 3, we show the numerical results and correlation of neutrino sector observables for both NO and IO of neutrino masses. We discuss our dark sector results in section 4 and show that the mass of DM candidates is very constrained. In section 5, we perform the numerical analysis for CLFV processes, and finally, concluding remarks are made in section 6.

2 Model SET-UP

We utilize a flavor-symmetric Dirac scotogenic model based on the A_4 symmetry group to account for neutrino oscillation parameters and DM phenomenology. In addition to the SM particles, we introduce BSM particles: scalars, η and ξ, which are SU$(2)_L$ doublet and singlet, respectively, and both transform as triplets under the A_4 symmetry. In this formalism, singlet fermions N_L and N_R are also introduced and transformed as triplets under the A_4 symmetry. We also add three right-handed neutrinos ν_R, which transform as singlets $(1, 1'', 1')$ under the A_4 symmetry. The SM Higgs doublet Φ transforms as trivial singlet (1), the charged lepton doublets L_i and singlets e_{R_i} $(i = 1, 2, 3)$ transform as $(1, 1', 1'')$ under the A_4 symmetry, respectively. For more details on the A_4 flavor symmetry and its multiplication rules, see appendix B. The particle content and their transformation rule under the SU$(2)_L \otimes$ U$(1)_Y$ are summarized in the second column of table 1. The last two columns present the transformation properties of different fields under the A_4 symmetry and the U$(1)_{B-L}$ as well as their residual subgroup $\mathcal{Z}_2$ and $\mathcal{Z}_3$, respectively. The charge assignments in table 1 ensure that, following the A_4 symmetry breaking by the VEVs of η and ξ, all the SM particles and ν_{R_i}'s remain even under the residual $\mathcal{Z}_2$ symmetry. In contrast, the triplet BSM particles may acquire

JHEP10(2025)088

Fields	$\mathrm{SU}(2)_L \otimes \mathrm{U}(1)_Y$	$A_4 \to \mathcal{Z}_2$	$\mathrm{U}(1)_{B-L} \to \mathcal{Z}_3$
L_i	(2, -1)	$(1, 1', 1'') \to (+, +, +)$	$-1 \to \omega^2$
e_{R_i}	(1, -2)	$(1, 1', 1'') \to (+, +, +)$	$-1 \to \omega^2$
H	(2, 1)	$1 \to +$	$0 \to 1$
ν_{R_i}	(1, 0)	$(1, 1'', 1') \to (+, +, +)$	$(-4, -4, 5) \to \omega^2$
N_L	(1, 0)	$3 \to (+, -, -)$	$-4 \to \omega^2$
N_R	(1, 0)	$3 \to (+, -, -)$	$-4 \to \omega^2$
η	(2, 1)	$3 \to (+, -, -)$	$3 \to 1$
ξ	(1, 0)	$3 \to (+, -, -)$	$0 \to 1$

Table 1. Field content and transformation properties of different fields under the $\mathrm{SU}(2)_L \otimes \mathrm{U}(1)_Y$, A_4, and $\mathrm{U}(1)_{B-L}$ symmetry, where $i = 1, 2, 3$ represents generation indices.

odd charges under the residual $\mathcal{Z}_2$ symmetry. The components of A_4 triplets η, ξ and N split into two, the first components transforming as even while the other components have odd charges under $\mathcal{Z}_2$, see appendix B for more details. The odd particles will eventually become dark sector particles as discussed in section 1. This discussion will focus on the scenario, where $\mathrm{U}(1)_{B-L}$ breaks down to the residual $\mathcal{Z}_3$ subgroup,[1] a natural outcome when the $B - L$ symmetry is broken in a unit of three. The presence of the residual $\mathcal{Z}_3$ subgroup ensures the Dirac nature of neutrinos.

Some of the salient features of the model are as follows:

- The dimension-4 Dirac neutrino mass term of the form, $\bar{L}_i \tilde{H} \nu_{R_j}$ and the bare Majorana mass term, $\bar{\nu}^c_{R_i} \nu_{R_j}$, are prohibited by both the A_4 and $\mathrm{U}(1)_{B-L}$ symmetries, except for $i = j = 1$. Specifically, although the terms $\bar{L}_1 \tilde{H} \nu_{R_1}$ and $\bar{\nu}^c_{R_1} \nu_{R_1}$ are allowed by A_4, they are forbidden due to the $\mathrm{U}(1)_{B-L}$ charge assignments.

- Similarly, the effective dimension-5 Weinberg operator $\bar{L}^c_i H H L_j$, which generates Majorana neutrino masses, is forbidden by both the A_4 and $\mathrm{U}(1)_{B-L}$ symmetries, except for $i = j = 1$. The term corresponding to $i = 1$ is allowed by the A_4 but remains forbidden by $\mathrm{U}(1)_{B-L}$ symmetry.

- The effective dimension-5 operator $\bar{L}_i H \nu_{R_j} \xi$, which generates Dirac neutrino masses, is forbidden by both the A_4 and $\mathrm{U}(1)_{B-L}$ symmetry.

- The effective dimension-5 operator $\bar{L}_i \, \eta \, \nu_{R_j} \, \xi$, where $i, j = 1, 2$ is allowed by the symmetries and requires UV-completion. This term emerges after the breaking of the A_4 symmetry, as shown in the top-right panel of figure 3.

[1]The explicit breaking of the $\mathrm{U}(1)_{B-L}$ symmetry arises from the cubic interaction term $H^\dagger \eta \xi$ in the scalar potential. Here, H and ξ carry zero $B - L$ charge, while η has a charge of three. Consequently, this interaction alters $B - L$ in steps of three, leading to the breaking of $\mathrm{U}(1)_{B-L}$ in units of three. As a result, the residual symmetry is the discrete subgroup $\mathcal{Z}_3$. Since $B - L$ is violated in multiples of three, the transformations that preserve the term $H^\dagger \eta \xi$ must correspond to those where $B - L$ charges differ by multiples of three. This implies that the $\mathrm{U}(1)_{B-L}$ phase factor, $e^{i\alpha(B-L)}$, is constrained such that $e^{i\alpha(B-L)} = e^{i\alpha(B-L+3n)}$ for any integer n. This periodicity signifies that the continuous $\mathrm{U}(1)_{B-L}$ symmetry is broken down to the discrete subgroup $\mathcal{Z}_3$.

JHEP10(2025)088

- In this minimal setup, one neutrino remains massless because the Yukawa interaction $Y'\bar{N}_L\xi\nu_R$ is forbidden for the third generation right-handed neutrino due to $B-L$ charge assignments. However, the massless neutrino can be made massive by adding a $\mathrm{SU}(2)_L$ singlet but A_4 triplet scalar ζ_9 with $B-L$ charge -9, allowing the Yukawa term $y_9\bar{N}_L\zeta_9\nu_{R_3}$. After SSB, ζ_9 acquires a VEV $(u_9,0,0)$ preserving the $A_4 \to \mathcal{Z}_2$ breaking. Then through the scoto-seesaw mechanism, we can generate a light Dirac neutrino mass for the (ν_{L_3},ν_{R_3}) pair. Note that, since one massless neutrino is allowed by the current oscillation data, we do not develop this analysis further.

The spontaneous breaking of the A_4 symmetry to its residual $\mathcal{Z}_2$ subgroup results in a hybrid scoto-seesaw mechanism, wherein an interplay between the tree level type-I seesaw and the one-loop level scotogenic mechanism facilitates the generation of neutrino masses. Moreover, the residual $\mathcal{Z}_2$ symmetry assumes the role of the scotogenic dark symmetry. Consequently, the lightest $\mathcal{Z}_2$ odd particle is inherently stable and emerges as a potential DM candidate.

2.1 Scalar sector

In this section, we discuss the scalar sector of our model and the emergence of $\mathcal{Z}_2$ dark symmetry from A_4 flavor symmetry. The scalar potential of our model is provided in appendix A. The A_4 symmetry is broken spontaneously by the VEVs of the scalars η, ξ. We aim to obtain the unbroken $\mathcal{Z}_2$ subgroup as a residual symmetry. This can be accomplished by the following VEV alignments of η and ξ components

$$\begin{aligned}\langle\eta_1\rangle &= \frac{v_2}{\sqrt{2}}, \ \langle\eta_2\rangle = 0 = \langle\eta_3\rangle\,,\\ \langle\xi_1\rangle &= u, \quad \ \langle\xi_2\rangle = 0 = \langle\xi_3\rangle\,.\end{aligned} \tag{2.1}$$

Under the residual $\mathcal{Z}_2$ symmetry, these fields transform as

$$\begin{aligned}\eta_1 &\to +\eta_1\,, \quad \eta_2 \to -\eta_2, \quad \eta_3 \to -\eta_3\,,\\ \xi_1 &\to +\xi_1\,, \quad \xi_2 \to -\xi_2, \quad \xi_3 \to -\xi_3\,.\end{aligned} \tag{2.2}$$

The SM H, being a singlet of A_4 transforms as $H \to +H$ under the residual $\mathcal{Z}_2$, and hence $\langle H\rangle = \frac{v_1}{\sqrt{2}}$. After the SSB, the $\mathrm{SU}(2)_L$ doublet scalars H, η_i and singlet scalar ξ_i can be expressed as

$$\begin{aligned}&H = \begin{pmatrix} H^+ \\ \frac{v_1+\phi_1+i\sigma_1}{\sqrt{2}}\end{pmatrix}, \quad \eta_1 = \begin{pmatrix} \eta_1^+ \\ \frac{v_2+\phi_2+i\sigma_2}{\sqrt{2}}\end{pmatrix}, \quad \eta_2 = \begin{pmatrix} \eta_2^+ \\ \frac{\eta_2^R+i\eta_2^I}{\sqrt{2}}\end{pmatrix}, \quad \eta_3 = \begin{pmatrix} \eta_3^+ \\ \frac{\eta_3^R+i\eta_3^I}{\sqrt{2}}\end{pmatrix},\\ &\xi_1 = u+\phi_3, \quad \xi_2 \equiv \xi_2^R, \quad \xi_3 \equiv \xi_3^R\,,\end{aligned} \tag{2.3}$$

where $\phi_1,\phi_2,\phi_3,\eta_2^R,\eta_3^R,\xi_2^R,\xi_3^R$ are CP even particles, whereas CP odd particles are $\sigma_1,\sigma_2,\eta_2^I,\eta_3^I$. The SM VEV is given by $\sqrt{v_1^2+v_2^2} = v_{\mathrm{SM}} \approx 246\,\mathrm{GeV}$.

One can compute the scalar mass spectrum from the scalar potential,

$$V = V_H + V_\eta + V_\xi + V_{H\eta} + V_{H\xi} + V_{\eta\xi} + V_{H\eta\xi} + \mathrm{h.c.}\,. \tag{2.4}$$

See eq. (A.2) in appendix A for the complete description of the potential. We want to mention that, unlike the scenario in ref. [26], the fields η_2 and η_3 do not mix in the present framework.

This distinction arises because, in this model, η is charged under $\mathrm{U}(1)_{B-L}$, which forbids terms such as $\eta^3 H$, ensuring that no mixing occurs between η_2 and η_3. The real component of the scalar η mixes with the real scalar ξ, with η_2^R mixing with ξ_2^R and η_3^R with ξ_3^R.

The mass matrices are given as follows:

$$\mathcal{M}_{2R}^2 = \begin{bmatrix} \Lambda_{\eta_2} v_2^2 - \alpha_2 u^2 & \alpha_1 v_2 u \\ \alpha_1 v_2 u & \Lambda_{\xi_2} u^2 - \alpha_3 v_2^2 \end{bmatrix}, \quad \mathcal{M}_{3R}^2 = \begin{bmatrix} \Lambda_{\eta_2} v_2^2 - \alpha_3 u^2 & \alpha_1 v_2 u \\ \alpha_1 v_2 u & \Lambda_{\xi_2} u^2 - \alpha_2 v_2^2 \end{bmatrix}. \tag{2.5}$$

The details about these mass matrices and the mass spectrum of other scalars of the model have been presented in the appendix A. The η_2^R mixes with ξ_2^R and after the mixing the mass eigenstates χ_1 and χ_2 are given as follows

$$\chi_1 = \cos\theta_2 \eta_2^R + \sin\theta_2 \xi_2^R, \quad \chi_2 = -\sin\theta_2 \eta_2^R + \cos\theta_2 \xi_2^R. \tag{2.6}$$

The mixing angle is given by

$$\tan 2\theta_2 = \frac{2\alpha_1 v_2 u}{\Lambda_{\xi_2} u^2 - \Lambda_{\eta_2} v_2^2 + \alpha_2 u^2 - \alpha_3 v_2^2}. \tag{2.7}$$

The mass eigenvalues corresponding to the mass eigenstates can be written as follows

$$\begin{aligned} m_{1R}^2 &= \left(\Lambda_{\eta_2} v_2^2 - \alpha_2 u^2\right) \cos^2\theta_2 + \left(\Lambda_{\xi_2} u^2 - \alpha_3 v_2^2\right) \sin^2\theta_2 - 2\alpha_1 v_2 u \sin\theta_2 \cos\theta_2, \\ m_{2R}^2 &= \left(\Lambda_{\eta_2} v_2^2 - \alpha_2 u^2\right) \sin^2\theta_2 + \left(\Lambda_{\xi_2} u^2 - \alpha_3 v_2^2\right) \cos^2\theta_2 + 2\alpha_1 v_2 u \sin\theta_2 \cos\theta_2. \end{aligned} \tag{2.8}$$

Similarly, η_3^R mixes with ξ_3^R and after the mixing the mass eigenstates χ_3 and χ_4 are given as follows

$$\chi_3 = \cos\theta_3 \eta_3^R + \sin\theta_3 \xi_3^R, \quad \chi_4 = -\sin\theta_3 \eta_3^R + \cos\theta_3 \xi_3^R. \tag{2.9}$$

The mixing angle in this case is given by

$$\tan 2\theta_3 = \frac{2\alpha_1 v_2 u}{\Lambda_{\xi_2} u^2 - \Lambda_{\eta_2} v_2^2 + \alpha_3 u^2 - \alpha_2 v_2^2}. \tag{2.10}$$

The mass eigenvalues corresponding to the mass eigenstates can be written as follows

$$\begin{aligned} m_{3R}^2 &= \left(\Lambda_{\eta_2} v_2^2 - \alpha_3 u^2\right) \cos^2\theta_3 + \left(\Lambda_{\xi_2} u^2 - \alpha_2 v_2^2\right) \sin^2\theta_3 - 2\alpha_1 v_2 u \sin\theta_3 \cos\theta_3, \\ m_{4R}^2 &= \left(\Lambda_{\eta_2} v_2^2 - \alpha_3 u^2\right) \sin^2\theta_3 + \left(\Lambda_{\xi_2} u^2 - \alpha_2 v_2^2\right) \cos^2\theta_3 + 2\alpha_1 v_2 u \sin\theta_3 \cos\theta_3. \end{aligned} \tag{2.11}$$

For a small mixing between the dark scalar particles, χ_1 and χ_3 will primarily behave as doublet scalars, while χ_2 and χ_4 will predominantly exhibit singlet nature. This follows from eqs. (2.6) and (2.9), which reduce to $\chi_{1,3} \sim \eta_{2,3}^R$ and $\chi_{2,4} \sim \xi_{2,3}^R$ in the limit of small mixing. Hence, in the scalar DM case, we will have two different types of DM candidates that will provide different natures of the DM particle (see section 4). For the sake of definiteness, we have taken χ_1 (χ_2) as doublet (singlet) DM candidates, making them the lightest particle in the dark sector. Note that taking χ_3 and χ_4 as a DM candidate will not change the results of our analysis.

JHEP10(2025)088

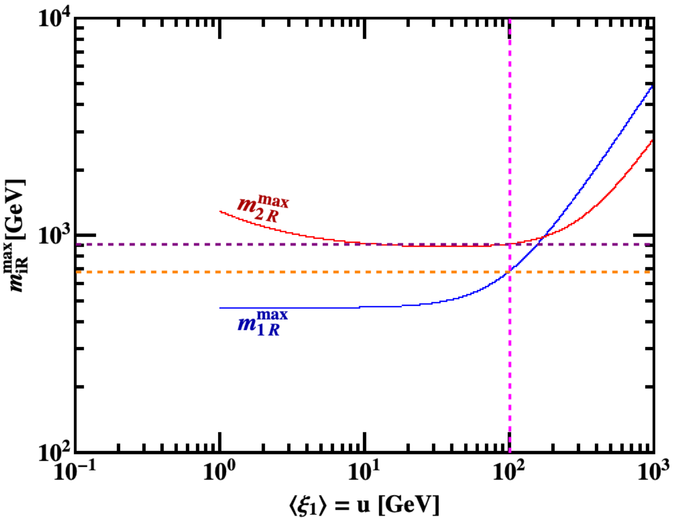

Figure 2. Correlation between the upper bound of dark sector scalar masses and singlet scalar VEV.

In figure 2, we have shown a correlation of the maximum value of the mass of dark sector particle, $m_{iR}^{\max}$, with the singlet scalar VEV, $\langle\xi_1\rangle = u$. The numerical values of other parameters are chosen such that m_{iR} is the maximum for a given value of u. Since, the doublets VEV follows $\sqrt{v_1^2+v_2^2} = v_{\rm SM}$ and λ has perturbativity limit, the maximum value of scalars masses (m_{iR}; $i = 1,2,3,4$) is governed by u. While performing the numerical analysis, we observed that there is an upper limit on u ($\sim 100\,$GeV), beyond which the neutrino oscillation data can no longer be explained, as discussed in section 3. The limit on u will restrict the dark scalar masses m_{1R} and m_{2R} to be ≈ 700 GeV,[2] and ≈ 900 GeV, respectively. A Similar behavior is observed for m_{3R} and m_{4R}, as their analytical expressions closely resemble those of m_{1R} and m_{2R}. Hence, the DM candidate in our model has an upper bound $\leq$ 700GeV.[3] This specific feature of our model arises directly from the $A_4 \to \mathcal{Z}_2$ breaking, distinguishing it from conventional Dirac scotogenic and scoto-seesaw models.

2.2 Yukawa sector

Referring to the charge assignments specified in table 1, the Yukawa Lagrangian governing the leptonic sector can be expressed as follows

$$\begin{aligned}-\mathcal{L}_y =\; & y_{11}(\overline{L}_1)_1 H(e_{R_1})_1 + y_{22}(\overline{L}_2)_{1''} H(e_{R_2})_{1'} + y_{33}(\overline{L}_3)_{1'} H(e_{R_3})_{1''} + y_1(\overline{L}_1)_1(\tilde{\eta}N_R)_1 \\ & + y_2(\overline{L}_2)_{1''}(\tilde{\eta}N_R)_{1'} + y_3(\overline{L}_3)_{1'}(\tilde{\eta}N_R)_{1''} + y_1'(\overline{N}_L\xi)_1(\nu_{R_1})_1 + y_2'(\overline{N}_L\xi)_{1'}(\nu_{R_2})_{1''} \\ & + M(\overline{N}_L N_R)_1 + \text{h.c.} \end{aligned} \tag{2.12}$$

Exploiting the A_4 multiplication rule (see appendix B), we can simplify eq. (2.12) as

$$\begin{aligned}-\mathcal{L}_y =\; & y_{11}\overline{L}_1 H e_{R_1} + y_{22}\overline{L}_2 H e_{R_2} + y_{33}\overline{L}_3 H e_{R_3} + y_1\overline{L}_1\left(\tilde{\eta}_1 N_{R_1} + \tilde{\eta}_2 N_{R_2} + \tilde{\eta}_3 N_{R_3}\right) \\ & + y_2\overline{L}_2\left(\tilde{\eta}_1 N_{R_1} + \omega\tilde{\eta}_2 N_{R_2} + \omega^2\tilde{\eta}_3 N_{R_3}\right) + y_3\overline{L}_3\left(\tilde{\eta}_1 N_{R_1} + \omega^2\tilde{\eta}_2 N_{R_2} + \omega\tilde{\eta}_3 N_{R_3}\right)\end{aligned}$$

[2]Note that, as pointed out in [26], scalar masses also have an upper bound, but this arises solely from the perturbativity constraint. In contrast, in the present model, the upper bound is determined by both the perturbativity limit and the restriction on the value of u imposed by neutrino observables.

[3]It is important to point out that even if the DM candidate is a fermion, this mass limit still applies as the DM candidate has to be the lightest in the dark sector particles.

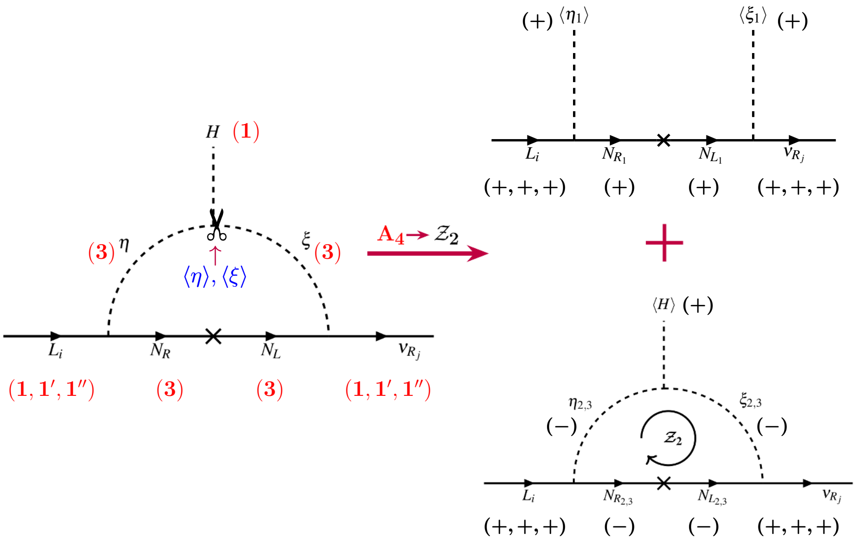

Figure 3. Breaking of $A_4 \to \mathcal{Z}_2$ leading to a scoto inverse-seesaw mass mechanism. The residual $\mathcal{Z}_2$ stabilizes the DM candidate running inside the loop. We have shown the A_4 ($\mathcal{Z}_2$) charges in the left (right) panel of the diagram.

$$
\begin{aligned}
&+ y_1' \left(\overline{N}_{L_1}\xi_1 + \overline{N}_{L_2}\xi_2 + \overline{N}_{L_3}\xi_3\right) \nu_{R_1} + y_2' \left(\overline{N}_{L_1}\xi_1 + \omega\overline{N}_{L_2}\xi_2 + \omega^2\overline{N}_{L_3}\xi_3\right) \nu_{R_2} \\
&+ M(\overline{N}_{L_1}N_{R_1} + \overline{N}_{L_2}N_{R_2} + \overline{N}_{L_3}N_{R_3}) + \text{h.c.}
\end{aligned}
\tag{2.13}
$$

where y_{ii}, y_i $(i = 1, 2, 3)$ and y_j', $(j = 1, 2)$ are the Yukawa couplings, ω is the cubic root of unity and M is the Dirac mass term of the BSM fermions. With this specific charge assignment, the mass matrix for charged leptons becomes diagonal. Consequently, the observed oscillation and mixing patterns of leptons originate solely from the neutrino sector as discussed next.

2.3 Neutrino masses

One of the primary objectives of the scoto-seesaw mechanism [8] is to account for the two observed neutrino mass-squared differences in oscillation experiments. To explain neutrino masses, we break the A_4 symmetry through the VEVs of η_1 and ξ_1. Consequently, this symmetry breaking divides the loop into two distinct segments: the type-I-like seesaw and the scoto-loop, as shown in figure 3. The A_4 ($\mathcal{Z}_2$) charges before (after) symmetry breaking are shown in figure 3. The breaking of the A_4 symmetry and the emergence of $\mathcal{Z}_2$ odd charges in the scoto-loop plays a very crucial role in generating neutrino masses and stabilizing the DM candidates. At the tree level, the (6×6) mass matrix in the basis $(\overline{\nu}_{L_i}, \overline{N}_{L_j})$ and $(\nu_{R_i}, N_{R_j})^T$, (where $i\,, j\; = 1, 2, 3)$ is given by

$$
\mathcal{M}_\nu = \begin{pmatrix}
0 & 0 & 0 & \frac{y_1 v_2}{\sqrt{2}} & 0 & 0 \\
0 & 0 & 0 & \frac{y_2 v_2}{\sqrt{2}} & 0 & 0 \\
0 & 0 & 0 & \frac{y_3 v_2}{\sqrt{2}} & 0 & 0 \\
y_1' u & y_2' u & 0 & M & 0 & 0 \\
0 & 0 & 0 & 0 & M & 0 \\
0 & 0 & 0 & 0 & 0 & M
\end{pmatrix},
\tag{2.14}
$$

JHEP10(2025)088

$$= \begin{pmatrix} 0 & \mathcal{M}_D \\ \boldsymbol{\mu} & \mathcal{M} \end{pmatrix} , \tag{2.15}$$

where,

$$\boldsymbol{\mu} = \begin{pmatrix} y_1'u & y_2'u & 0 \\ 0 & 0 & 0 \\ 0 & 0 & 0 \end{pmatrix} , \ \mathcal{M}_D = \frac{1}{\sqrt{2}} \begin{pmatrix} y_1 v_2 & 0 & 0 \\ y_2 v_2 & 0 & 0 \\ y_3 v_2 & 0 & 0 \end{pmatrix} , \ \mathcal{M} = \begin{pmatrix} M & 0 & 0 \\ 0 & M & 0 \\ 0 & 0 & M \end{pmatrix} . \tag{2.16}$$

Now, in the limit, $M \gg y_j'u,\ y_i v_2$ ($j = 1, 2$ and $i = 1, 2, 3$), the light Dirac neutrino mass matrix can be written as

$$-m_\nu^{(1)} = \mathcal{M}_D \mathcal{M}^{-1} \boldsymbol{\mu} = \frac{v_2 u}{\sqrt{2} M} \begin{pmatrix} y_1 y_1' & y_1 y_2' & 0 \\ y_2 y_1' & y_2 y_2' & 0 \\ y_3 y_1' & y_3 y_2' & 0 \end{pmatrix} . \tag{2.17}$$

The resulting neutrino mass is proportional to the $\boldsymbol{\mu}$-matrix, where u is the VEV of the singlet field ξ. Since u can take very small values, this feature is characteristic of the inverse seesaw mechanism [36], which will be discussed in the next section. It is noteworthy that the rank of $m_\nu^{(1)}$ is one, implying that only one of the neutrinos acquires mass at the tree level.

Note that, even when we take the one-loop contribution associated with N_1 into account, the texture zeros of eq. (2.17) remain symmetry protected. This results in an additional mass matrix with a similar structure to eq. (2.17). It is due to the fact that the residual $\mathcal{Z}_2$ symmetry remains unbroken, and as a consequence, mixing between the first generation singlet fermion N_1 (even under $\mathcal{Z}_2$) and the other generations N_2, N_3 (odd under $\mathcal{Z}_2$) is forbidden. Similarly, mixing between scalars η_1 or ξ_1 (even under $\mathcal{Z}_2$) and the dark scalars $\eta_{2,3}$ or $\xi_{2,3}$ (odd under $\mathcal{Z}_2$) are also not allowed by this residual symmetry. As a result, the loop correction do not induce any new non-zero entries in the neutrino mass matrix; the zero entries remain protected by symmetry. The loop induced corrections affect only the non-zero elements of the tree-level mass matrix in eq. (2.17), which can be effectively absorbed into a redefinition of the Yukawa couplings. We do not explicitly include these loop contribution in our analysis. Thus, the overall structure of the mass matrix remains unchanged and only one neutrino mass can be generated at this stage.

The additional neutrino masses can be generated at the loop level from the scoto-loop mechanism. The loop contribution is given by

$$(\mathcal{M}_\nu)_{ij} = \sum_{k=1}^{3} Y_{ik} Y'_{jk} (c_2 + c_3) , \tag{2.18}$$

where, Y_{ik} and Y'_{jk} are Yukawa couplings and

$$\begin{aligned} c_2 &= \frac{M}{32\pi^2} \sin(2\theta_2) \left[\frac{m_{1R}^2}{m_{1R}^2 - M^2} \ln\left(\frac{m_{1R}^2}{M^2}\right) - \frac{m_{2R}^2}{m_{2R}^2 - M^2} \ln\left(\frac{m_{2R}^2}{M^2}\right) \right] , \\ c_3 &= \frac{M}{32\pi^2} \sin(2\theta_3) \left[\frac{m_{3R}^2}{m_{3R}^2 - M^2} \ln\left(\frac{m_{3R}^2}{M^2}\right) - \frac{m_{4R}^2}{m_{4R}^2 - M^2} \ln\left(\frac{m_{4R}^2}{M^2}\right) \right] . \end{aligned} \tag{2.19}$$

The Yukawa couplings Y_{ik} and Y'_{jk} are as follows

$$\begin{aligned}
&Y_{11}=y_1, \quad Y_{12}=y_1, \quad Y_{13}=y_1, \quad Y_{21}=y_2, \quad Y_{22}=\omega y_2, \quad Y_{23}=\omega^2 y_2\,,\\
&Y_{31}=y_3, \quad Y_{32}=\omega^2 y_3, \quad Y_{33}=\omega y_3\,,\\
&Y'_{11}=y'_1, \quad Y'_{12}=y'_1, \quad Y'_{13}=y'_1, \quad Y'_{21}=y'_2, \quad Y'_{22}=\omega y'_2, \quad Y'_{23}=\omega^2 y'_2\,.
\end{aligned} \tag{2.20}$$

Hence, from the loop contribution, the neutrino mass matrix elements are given by

$$\begin{aligned}
&(\mathcal{M}_\nu)_{11}=y_1y'_1\,(c_2+c_3)\,, \quad (\mathcal{M}_\nu)_{12}=y_1y'_2\left(\omega c_2+\omega^2 c_3\right), \quad (\mathcal{M}_\nu)_{13}=0\,,\\
&(\mathcal{M}_\nu)_{21}=y_2y'_1\left(\omega c_2+\omega^2 c_3\right), \quad (\mathcal{M}_\nu)_{22}=y_2y'_2\left(\omega^2 c_2+\omega c_3\right), \quad (\mathcal{M}_\nu)_{23}=0\,,\\
&(\mathcal{M}_\nu)_{31}=y_3y'_1\left(\omega^2 c_2+\omega c_3\right), \quad (\mathcal{M}_\nu)_{32}=y_3y'_2\,(c_2+c_3)\,, \quad (\mathcal{M}_\nu)_{33}=0\,.
\end{aligned} \tag{2.21}$$

Thus, the light neutrino mass matrix arising from the scoto-loop level can be expressed as

$$m_\nu^{(2)}=\begin{pmatrix} y_1y'_1d_1 & y_1y'_2d_2 & 0\\ y_2y'_1d_2 & y_2y'_2d_3 & 0\\ y_3y'_1d_3 & y_3y'_2d_1 & 0\end{pmatrix}, \tag{2.22}$$

where, $d_1=c_2+c_3$, $d_2=\omega c_2+\omega^2 c_3$, and $d_3=\omega^2 c_2+\omega c_3$. Combining the contributions originating from both the tree-level seesaw and the scoto-loop, known as the "scoto-seesaw" scenario, yields the expression for the light neutrino mass matrix as follows:

$$m_\nu^{(TOT)}=m_\nu^{(1)}+m_\nu^{(2)}\equiv\begin{pmatrix} y_1y'_1\left(d_1-\frac{v_2u}{\sqrt{2}M}\right) & y_1y'_2\left(d_2-\frac{v_2u}{\sqrt{2}M}\right) & 0\\ y_2y'_1\left(d_2-\frac{v_2u}{\sqrt{2}M}\right) & y_2y'_2\left(d_3-\frac{v_2u}{\sqrt{2}M}\right) & 0\\ y_3y'_1\left(d_3-\frac{v_2u}{\sqrt{2}M}\right) & y_3y'_2\left(d_1-\frac{v_2u}{\sqrt{2}M}\right) & 0\end{pmatrix}. \tag{2.23}$$

In the matrix $m_\nu^{(TOT)}$, d_1 is a real parameter whereas d_2 and d_3 are complex and conjugate to each other due to the presence of ω. Due to the $U(1)_{B-L}$ charge assignment (see table 1), ν_{R_3} has been decoupled. Therefore, it is evident that within our model, only two neutrinos acquire mass, while one remains massless. This finding remains consistent with the neutrino oscillation data.

3 Neutrino sector predictions

In this section, we discuss the numerical results concerning the neutrino sector. We start by analyzing the features of neutrino mass matrices in our model. The tree-level neutrino mass matrix given in eq. (2.17) is proportional to the factor u/M. In this model, ξ being a singlet of $SU(2)_L$, its VEV $\langle\xi\rangle=u$ can be chosen arbitrarily. Note that in the type-I seesaw mechanism, right-handed neutrino masses are typically around $\sim 10^{12}$ GeV for $\mathcal{O}(1)$ Yukawa couplings. In contrast, within this framework, the freedom to choose the value of u allows us to reduce the fermion mass M to a desired value while maintaining a fixed u/M ratio. This is similar to the inverse seesaw mass mechanism [35], where a small fermion mass is achieved by introducing a small μ parameter, often referred to as the lepton number violating parameter. In our framework, this scenario is realized by inducing a VEV for

JHEP10(2025)088

ξ, leading us to refer to it as the "*inverse seesaw*" mass mechanism. As discussed earlier, the two mass-squared differences, $\Delta m^2_{\rm sol}$ and $\Delta m^2_{\rm atm}$, are generated at the loop level (via the scotogenic mechanism) and tree level, respectively. Due to the A_4 symmetry in our model, both the loop and tree level contributions involve the same Yukawa couplings. For $\mathcal{O}(1)$ Yukawa couplings, the mass parameter M is bounded from above (typically $\sim$ a few TeV), which also constrains the VEV u (to $\sim 100\,$GeV) to simultaneously satisfy both the mass-squared differences. This upper bound on u has direct implications for the scalar mass spectrum, as illustrated in figure 2, and significantly affects the "dark sector" by restricting the parameter space available for viable DM candidates (see section 4).

We now turn to the numerical analysis of the neutrino sector. For our analysis, we consider two benchmark scenarios:

$$\begin{aligned}
&\text{Case}-\text{I}: y_1 = y_1' \,\text{and}\, y_2 = y_2'\,,\\
&\text{Case}-\text{II}: y_3 = \epsilon\, y_2, \epsilon = (0,1)\,.
\end{aligned} \tag{3.1}$$

It is worth noting that our analysis is consistent with the latest global fit data [5–7]. In our model, one of the neutrinos is massless. Once the constraints from the two mass-squared differences are imposed, the neutrino mass spectrum becomes fully determined for both normal ordering (NO) and inverted ordering (IO). This prediction of a massless neutrino also leads to precise predictions for other neutrino sector observables in both NO and IO cases, as we discuss below.

3.1 Normal ordering

For NO, $m_3 > m_2 > m_1$ and as the $m_1 = 0$ in our scenario, we find m_3 and m_2 using global-fit data [5–7] as

$$\begin{aligned}
&\Delta m^2_{31} = 2.55\times 10^{-3}\ \text{eV}^2, \quad \Delta \text{m}^2_{21} = 7.5\times 10^{-5}\ \text{eV}^2\,,\\
&\implies \quad m_3 = 5.05\times 10^{-2}\ \text{eV}, \quad \text{m}_2 = 8.66\times 10^{-3}\ \text{eV}\,.
\end{aligned} \tag{3.2}$$

Sum of neutrino masses confined to a narrow range, $\sum m_i \in [0.058, 0.061]\,$eV, which we obtain by varying Δm^2_{ij} into their 3σ ranges [5–7]. This value is consistent with the Planck data [3] as well as with the recent DESI result [40]. Furthermore, the effective neutrino mass $\langle m_\beta\rangle$ is defined as:

$$\langle m_\beta\rangle \equiv \sqrt{\sum_j |U_{ej}|^2 m_j^2} = \sqrt{c_{12}^2c_{13}^2m_1^2 + s_{12}^2c_{13}^2m_2^2 + s_{13}^2m_3^2}\,, \tag{3.3}$$

where $c_{ij} = \cos\theta_{ij}$ and $s_{ij} = \sin\theta_{ij}$ and that falls in the range $\langle m_\beta\rangle \in [8.26, 9.57]\,$meV. This value is consistent with the expected sensitivity of KATRIN [41]. In addition to the constrained values of both $\sum m_i$ and $\langle m_\beta\rangle$, they exhibit a correlation with each other as shown in figure 4. Predictions for the CP-violating phase $\delta_{\rm CP}$ and its correlation with the atmospheric mixing angle θ_{23} are displayed in the left panel of figure 5 for case-I, while the prediction for case-II is shown in the right panel. For comparison, the latest global analysis of neutrino oscillation data [6] is included, represented by the cyan-colored contours in figure 5, with the best-fit value indicated by a black dot.

JHEP10(2025)088

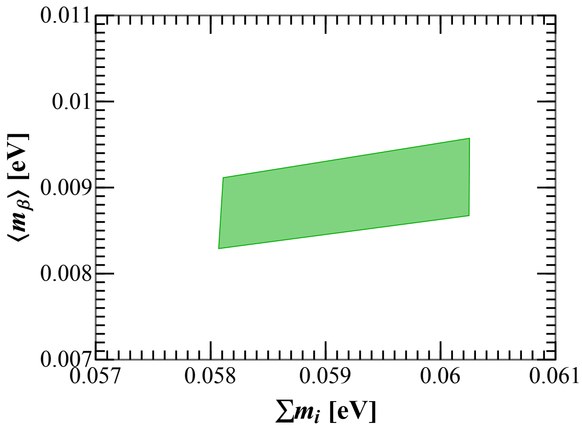

Figure 4. Correlation between sum of neutrino masses $\sum m_i$ and effective mass $\langle m_\beta \rangle$ of beta decay in the NO case.

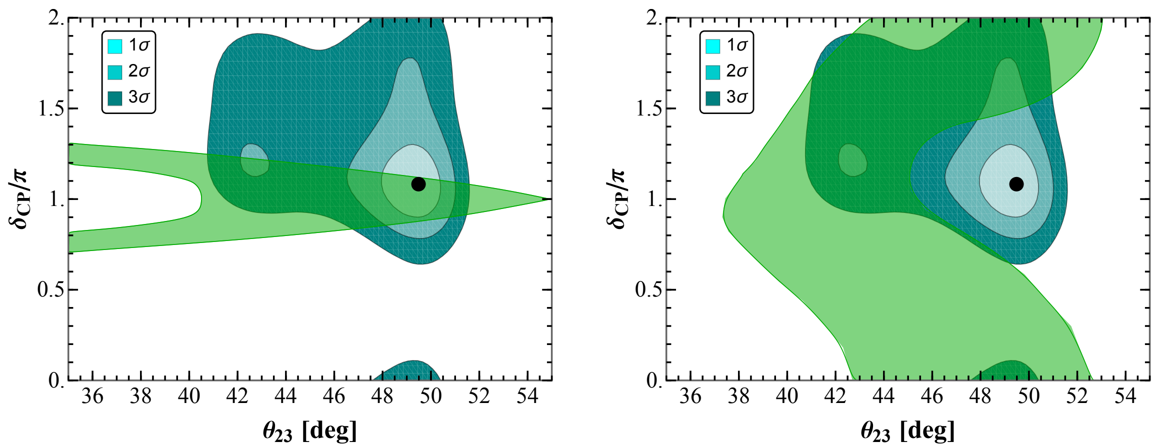

Figure 5. Correlation between $\delta_{\rm CP}$ and θ_{23} for NO, where left (right)-panel represents case-I (-II).

From case-I, we observe a sharp and well-defined correlation between the CP-violating phase $\delta_{\rm CP}$ and the atmospheric mixing angle θ_{23}, with predictions clustering closely around the global best-fit value, i.e., $\delta_{\rm CP} \sim \pi$. Interestingly, this correlation exhibits a bifurcated structure, with two distinct branches centered near $\delta_{\rm CP} = \pi$. Notably, this case excludes CP-conserving values ($\delta_{\rm CP} = \pi$) for a portion of the lower octant, specifically for $\theta_{23} \leq 42^\circ$. Furthermore, the latest global analysis of neutrino oscillation data disfavors the model predictions for $\theta_{23} \lesssim 41^\circ$ and $\theta_{23} \gtrsim 51^\circ$. In contrast, for case-II, the model predictions are found to be incompatible with the global-fit data at the $1\,\sigma$ confidence level. In particular, the CP-violating phase values in the range $0.1\pi \lesssim \delta_{\rm CP} \lesssim 0.7\pi$ are disfavored even at the $3\,\sigma$ confidence level. However, the model remains viable at the $2\,\sigma$ confidence level when the CP values lie in the second or the third quadrants, offering a window for experimental verification in future neutrino oscillation studies.

JHEP10(2025)088

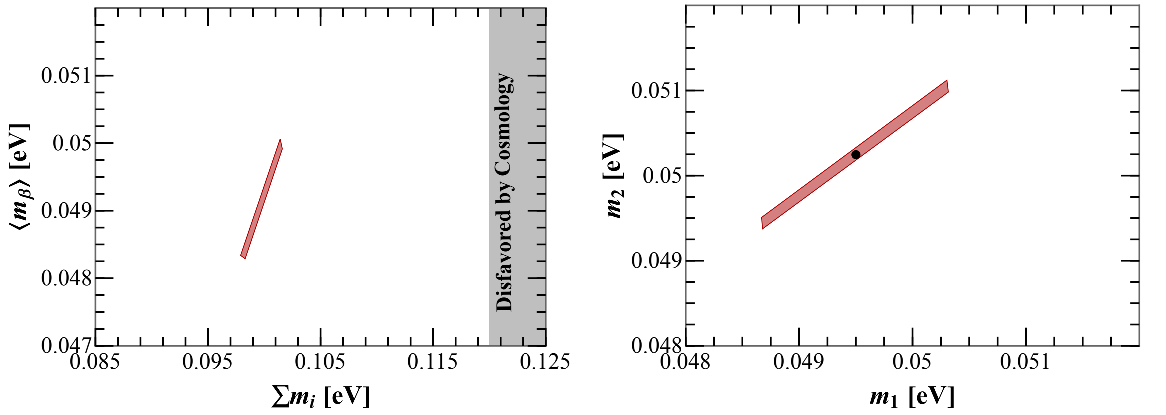

Figure 6. Model Predictions in the IO case. *Left panel*: correlation between $\sum m_i$ and $\langle m_\beta \rangle$. The gray band depicts the cosmology limit. *Right panel:* correlation between neutrino masses, m_1 and m_2.

3.2 Inverted ordering

For IO, it is noteworthy that, unlike the Majorana case [26], where IO was forbidden, in this Dirac neutrino formalism, IO is permitted and remains consistent with the observed neutrino oscillation data. As in IO, neutrino mass ordering follows $m_2 > m_1 > m_3$, hence the lightest one, $m_3 = 0$ for this case. Imposing Δm^2_{ij} constraint, we find m_1 and m_2 are as follows:

$$\begin{aligned} &\Delta m^2_{31} = -2.45 \times 10^{-3}\ \mathrm{eV}^2, \quad \Delta \mathrm{m}^2_{21} = 7.5 \times 10^{-5}\ \mathrm{eV}^2\,, \\ &\Longrightarrow \qquad m_1 = 4.950 \times 10^{-2}\ \mathrm{eV}, \quad \mathrm{m}_2 = 5.025 \times 10^{-2}\ \mathrm{eV}\,. \end{aligned} \tag{3.4}$$

In this case, we also find stringent range values for the sum of neutrino masses $\sum m_i$ and the effective mass of the beta decay $\langle m_\beta \rangle$ and are given as follows:

$$\sum m_i \in [0.098, 0.101]\,\mathrm{eV}, \quad \langle \mathrm{m}_\beta \rangle \in [0.048, 0.050]\,\mathrm{eV}\,,$$

which are consistent with the Planck results [3] and expected sensitivity of KATRIN [41], respectively. In the left panel of figure 6, we show the correlation of $\sum m_i$ and $\langle m_\beta \rangle$ with each other. In addition, there is a strong correlation between neutrino masses m_1 and m_2 as shown in the right panel of figure 6. Note that, unlike the NO, where $m_1 = 0 \simeq m_2$, leading to no observable correlation, the IO has $m_3 = 0$ with m_1 and m_2 being relatively large, resulting in a strong correlation between them.

In figure 7, we present the correlation between δ_{CP} and θ_{23} in the case of IO, for the two benchmark scenarios defined in eq. (3.1). From the left panel, corresponding to case-I, we observe a pattern where the model predicts two distinct branches of solutions for δ_{CP}. However, one of these branches is excluded by the latest global analysis of neutrino oscillation data. The parameter space consistent with current experimental constraints can be summarized as $\theta_{23} \in [41^\circ, 51^\circ]$ and $\delta_{\mathrm{CP}} \in [1.5\pi, 2\pi]$. In the right panel, which shows case-II, we find that the model predicts a broader range of allowed values for δ_{CP} compared to case-I. Specifically, the compatible region extends over $\delta_{\mathrm{CP}} \in [0.9\pi, 2\pi]$, while the allowed range for θ_{23} remains similar to that of case-I. This suggests that case-II is more flexible in accommodating current neutrino data within the IO scenario.

JHEP10(2025)088

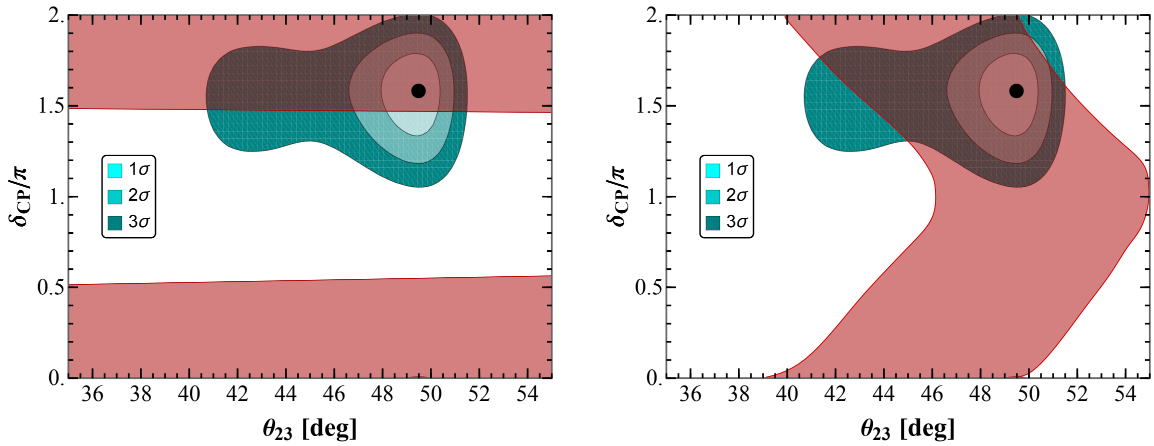

Figure 7. Same as figure 5, but for IO.

4 Dark sector results

We now turn our attention to the DM phenomenology of our model. In the early universe, all the particles in the dark sector are in thermal equilibrium with the SM fields due to the production-annihilation processes depicted in appendix C. As the universe expands and cools, the temperature drops. For unstable particles, there is a threshold temperature below which the thermal bath lacks sufficient energy to produce them, while their annihilation and decay processes continue, leading to their eventual disappearance. However, the lightest particle of the dark sector remains stable. Once this stable particle decouples from the thermal bath, its relic density becomes 'freezed out'. This relic density can be computed and compared with observations from the Planck satellite data [3]. The current observed value for the DM relic density, as measured by Planck data, is $0.1126 \leq \Omega h^2 \leq 0.1246$ at the 3σ confidence level [3]. This class of DM candidates could potentially be probed through nuclear recoil experiments such as XENONnT [42] and LZ [43]. In our model, we have both scalar and fermionic DM candidates. In the scalar sector, the viable DM candidates include the lightest neutral, predominantly doublet dark scalars ($\chi_{1,3}$), as well as the predominantly singlet dark scalars ($\chi_{2,4}$). On the other hand, the fermionic DM candidates are represented by the neutral fermions ($N_{2,3}$). The stability of the lightest dark sector particle is ensured by the residual $\mathcal{Z}_2$ symmetry.

As we have discussed in section 2.1, the mass of the scalar is related to the VEV of the singlet scalar (u) as shown in figure 2. From the neutrino sector analysis, we find that there is an upper bound for $u \sim 100\,\text{GeV}$. This limit of VEV restricts the dark scalar mass to be around 700 GeV. Hence, in our model, the mass of the DM can not be greater than this value. Here, we would like to mention that in our numerical analysis of the dark sector as well as in LFV, we have presented the general scan and then shaded the region with the red color, which is not allowed by the neutrino oscillation constraints.

Furthermore, we have imposed the collider constraint from LHC and LEP (LEP-I and LEP-II), which have a significant impact on the viable parameter space of the DM mass.

JHEP10(2025)088

Parameter	Range	Parameter	Range
λ_1	$[10^{-4}, \sqrt{4\pi}]$	λ_{η_l}	$[10^{-8}, \sqrt{4\pi}]$
λ_{ξ_k}	$[10^{-8}, \sqrt{4\pi}]$	$\lvert\lambda_{H\eta_i}\rvert$	$[10^{-8}, \sqrt{4\pi}]$
$\lvert\lambda_{H\xi_m}\rvert$	$[10^{-8}, \sqrt{4\pi}]$	$\lvert\lambda_{\eta\xi_n}\rvert$	$[10^{-8}, \sqrt{4\pi}]$
$\lvert\kappa\rvert$	$[10^{-8}, 30]$ GeV	u	$[10^{-4}, 10^{5}]$ GeV
M_{N_i}	$[10, 10^{12}]$ GeV	$y_i,\, y'_j$	$[10^{-6}, 10^{-1}]$

Table 2. The ranges of values used in the numerical scan for the dark sector results correspond to the indices $i = 1, 2, 3,\ j = 1, 2,\ k = 1, 2, 3, 4, 5,\ l = 1, 2, 3, 4, 6, 7, 9, 10, 11, 12,\ m = 1, 2,$ and $n = 1, 2, 4, 5, 8, 9, 11, 12, 14$, as defined in the scalar potential given in appendix A.

- *The most important LHC limit comes from the possibility of Higgs' "invisible decay" to dark sector particles. The Higgs invisible decay comes through the channel $h_1 \to \chi_i\chi_j$ $(i, j = 1, 2, 3, 4)$. The current bound for the branching ratio of the Higgs invisible decay from LHC data has a limit [44]:*

$$BR(h_1 \to inv) < 0.145. \tag{4.1}$$

- *The LEP-I measurements rule out SM gauge boson decays into dark sector particles [45, 46]. This condition leads to the following lower limit on the dark sector scalar masses:*

$$m_{\eta^{R/I}_{2/3}} + m_{\eta^{\pm}_{2/3}} > M_W, \quad m_{\eta^{R}_{2/3}} + m_{\eta^{I}_{2/3}} > M_Z, \quad m_{\eta^{\pm}_{2/3}} + m_{\eta^{\mp}_{2/3}} > M_Z\,. \tag{4.2}$$

- *Chargino searches in LEP-II in the context of singly-charged scalar production $e^+e^- \to \eta^{\pm}_{2/3}\eta^{\mp}_{2/3}$ can be adapted to our analysis to set the limits [47] given by*

$$m_{\eta^{\pm}_{2/3}} > 70\ \text{GeV}\,. \tag{4.3}$$

We performed a detailed numerical scan with input parameters given in table 2.

In appendix C, we present the relevant Feynman diagrams corresponding to the annihilation and co-annihilation channels that contribute to the relic density of the DM candidate. Additionally, we include diagrams associated with the direct detection (DD) prospects of the DM. For scalar DM, direct detection occurs at the tree level via Higgs and Z-boson exchange. In contrast, fermionic DM does not couple directly to the quarks at the tree level, and its DD interactions arise only at the loop level.

4.1 Doublet scalar DM

Results for the doublet scalar DM (χ_1) are discussed in this section. Note that considering χ_3 as a DM candidate will have the same results as the DM candidate χ_1. In the left panel of figure 8, the dependence of the DM relic density on the mass of the doublet DM m_{1R} has been shown. The blue points represent the 3σ range of the relic density for doublet DM as measured by the Planck collaboration. The olive green and gray points represent the over-abundant and under-abundant relic density, respectively. Our analysis reveals that the blue points span a wide mass range from 10 GeV to approximately 3 TeV. The right side of

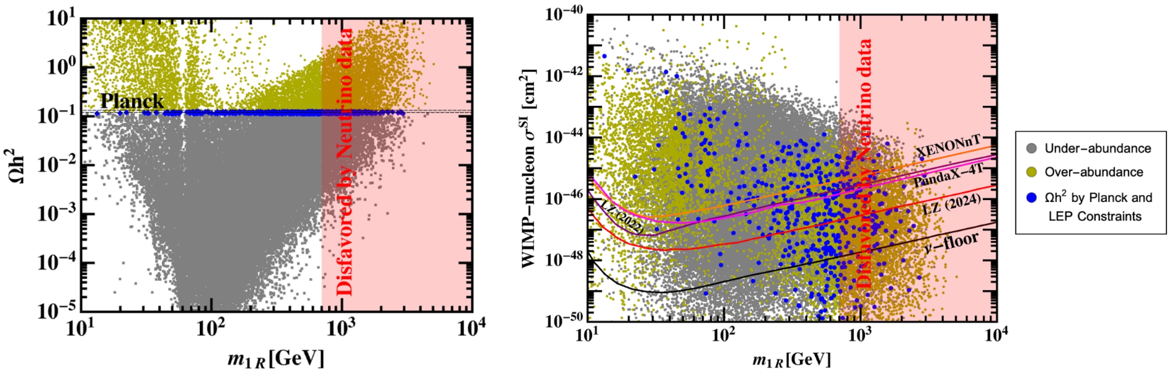

Figure 8. Predictions for the doublet DM candidate χ_1. The left panel shows relic density and the right panel shows WIMP-nucleon cross section vs doublet scalar DM mass m_{1R}. The red shaded region is constrained by neutrino oscillation data.

figure 8 illustrates the relationship between the spin-independent WIMP-nucleon cross-section and the mass of the DM particle. Various colored lines in figure 8 denote the latest DD upper bounds from the XENONnT collaboration [42], the LZ collaboration [43, 48], and the PandaX-4T collaboration [49]. The black line signifies the lower limit corresponding to the "neutrino floor" arising from coherent elastic neutrino scattering [50]. Observing the right panel of figure 8, one can deduce that the blue points positioned below the constraints of LZ are considered permissible based on considerations of relic density, LHC, LEP, and DD constraints. Apart from these constraints, the DM mass has an upper bound $\sim 700\,\text{GeV}$ (see figure 2). Note that we pointed out in figure 2 that neutrino data could not be explained for DM mass greater than 700 GeV, which we show by the red shaded region. Therefore, the shaded region is ruled out for DM by neutrino oscillation constraints. Moreover, the mass region up to around 85 GeV is excluded by collider constraints from the LHC and LEP. Consequently, the doublet DM mass region is confined in the range $85 \leq m_{1R} \leq 700\,\text{GeV}$, satisfying neutrino, DM, as well as collider constraints.

4.2 Singlet scalar DM

We now consider the scenario in which the DM is primarily composed of the $\text{SU}(2)_L$ singlet scalar, identified as $\chi_{2,4}$. In the following, we present our results for the DM candidate χ_2, representing the singlet scalar case, noting that the analysis and results for χ_4 are qualitatively similar. The left panel of figure 9 shows the dependence of the DM relic density on the DM mass m_{2R}. The color code remains the same as for the doublet scalar DM case. In our analysis, we observe that for the singlet DM candidate, the correct relic density points range from 20 GeV to 10 TeV of the DM mass. Hence, again constraining them from neutrino oscillation, DM constraints, and collider constraints, the allowed mass region for singlet DM is $20 \leq m_{2R} \leq 700\,\text{GeV}$.

4.3 Fermionic DM

The results for the fermionic DM are presented in figure 10, demonstrating that the fermionic DM is consistent with all current experimental constraints. When the mass of the dark fermion

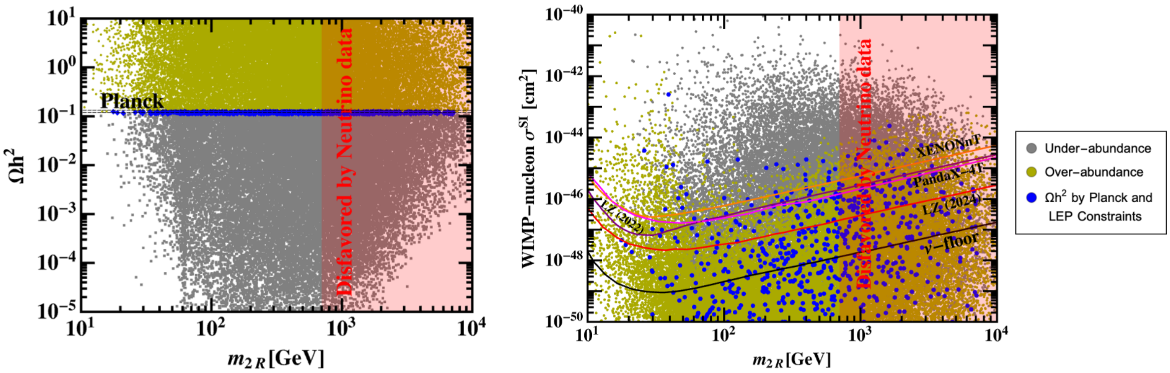

Figure 9. Predictions for the singlet scalar DM candidate χ_2. The left panel shows relic density and the right panel shows WIMP-nucleon cross section vs singlet scalar DM mass m_{2R}.

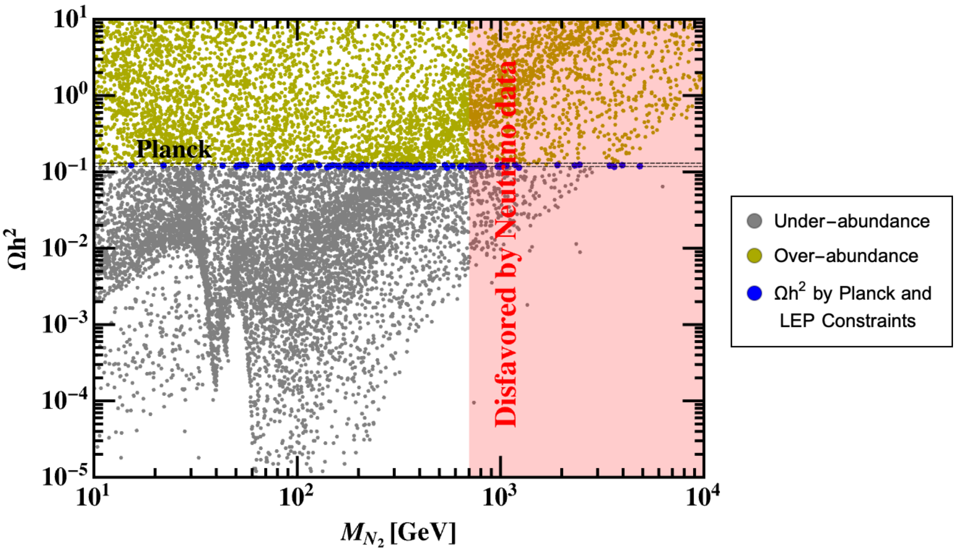

Figure 10. Relic density as a function of fermionic DM mass M_{N_2} has been presented.

is significantly smaller than that of the neutral doublet and singlet scalar, co-annihilation channels contribute negligibly to the computation of relic density. Consequently, the relic density is predominantly determined by fermion annihilation channels alone, leading to a higher relic density. This behavior can be understood by looking at figure 8 of the ref. [26]. To achieve the correct relic density, it is crucial to account for co-annihilation channels as well.

Importantly, it is observed that for the fermionic DM, the limitations from DD experiments such as XENONnT, LZ, and PandaX-4T are not significant. This is attributed to the fact that the fermionic DM candidate has no direct interaction with quarks at the tree level. It is noteworthy that, within the parameter space explored, the fermionic DM candidate N_2 with a mass range between 10 GeV to 5 TeV concurrently satisfies all the previously discussed constraints. Again, implementing the neutrino oscillation constraints, this region will be further narrowed down to the $10 \leq M_{N_2} \leq 700\,\text{GeV}$.

JHEP10(2025)088

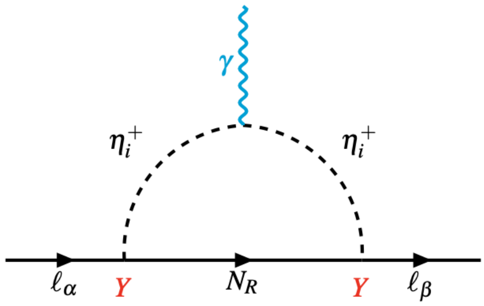

Figure 11. One loop feynman diagram for the process $\ell_\alpha \to \ell_\beta\gamma$.

5 Charged lepton flavor violation

The discovery of neutrino oscillations provides compelling evidence for the existence of charged lepton flavor violating interactions [51]. In the SM, if neutrino masses originate similarly to those of other fermions (via Yukawa interactions with the SM Higgs), charged lepton flavor violating (CLFV) rates are expected to be extremely suppressed to practically unobservable levels. For instance, the branching fraction for $\mu \to e\gamma$ decay is estimated to be of the order of 10^{-54}, significantly below the sensitivity threshold of any feasible experiment. However, alternative mechanisms for neutrino mass generation could yield to potentially significant CLFV effects. Extensive experimental efforts have been made to explore flavor-violating decays of muons and tau leptons. Yet, as of the present date, no conclusive positive signals have emerged from these experiments. Consequently, the absence of such signals has prompted the establishment of stringent bounds on the branching ratios associated with these flavor-violating decay processes. Presently, these limits stand at $BR(\mu \to e\gamma) < 3.1 \times 10^{-13}$ [52], $BR(\tau \to e\gamma) < 3.3 \times 10^{-8}$ [53], and $BR(\tau \to \mu\gamma) < 4.2 \times 10^{-8}$ [54], respectively. Projections indicate significant enhancements in the near future for detecting these decay processes, with anticipated limits of $BR(\mu \to e\gamma) < 6 \times 10^{-14}$ [55], $BR(\tau \to e\gamma) < 9 \times 10^{-9}$ [56], and $BR(\tau \to \mu\gamma) < 6.9 \times 10^{-9}$ [56], respectively. The leading contribution to $\ell_\alpha \to \ell_\beta\gamma$ arises at the one-loop level through the mediation of the charged scalar η_i^+ as shown in the diagram of figure 11. The branching ratio of this process is given by

$$\mathrm{Br}(\ell_\alpha \to \ell_\beta\gamma) = \mathrm{Br}\left(\ell_\alpha \to \ell_\beta \nu_\alpha \overline{\nu_\beta}\right) \times \frac{3\alpha_{em}}{16\pi G_F^2} \left| \sum_i \frac{Y_{\beta i} Y_{\alpha i}^*}{m_{\eta_i^+}^2} j\left(\frac{M_{N_i}^2}{m_{\eta_i^+}^2}\right) \right|^2 . \tag{5.1}$$

We take the numerical values of $\mathrm{Br}\left(\ell_\alpha \to \ell_\beta \nu_\alpha \overline{\nu_\beta}\right)$, α_{em} and G_F from the PDG [57] and $j(x)$ is the loop function defined as

$$j(x) = \frac{1 - 6x + 3x^2 + 2x^3 - 6x^2 \log(x)}{12(1-x)^4} . \tag{5.2}$$

We have analyzed various CLFV rates corresponding to different DM candidates. In figure 12, we show the resulting CLFV decay rates as a function of the mass for each viable DM candidate in our model. The gray and olive green points represent regions of under-abundance and over-abundance, respectively, while the blue points correspond to the correct

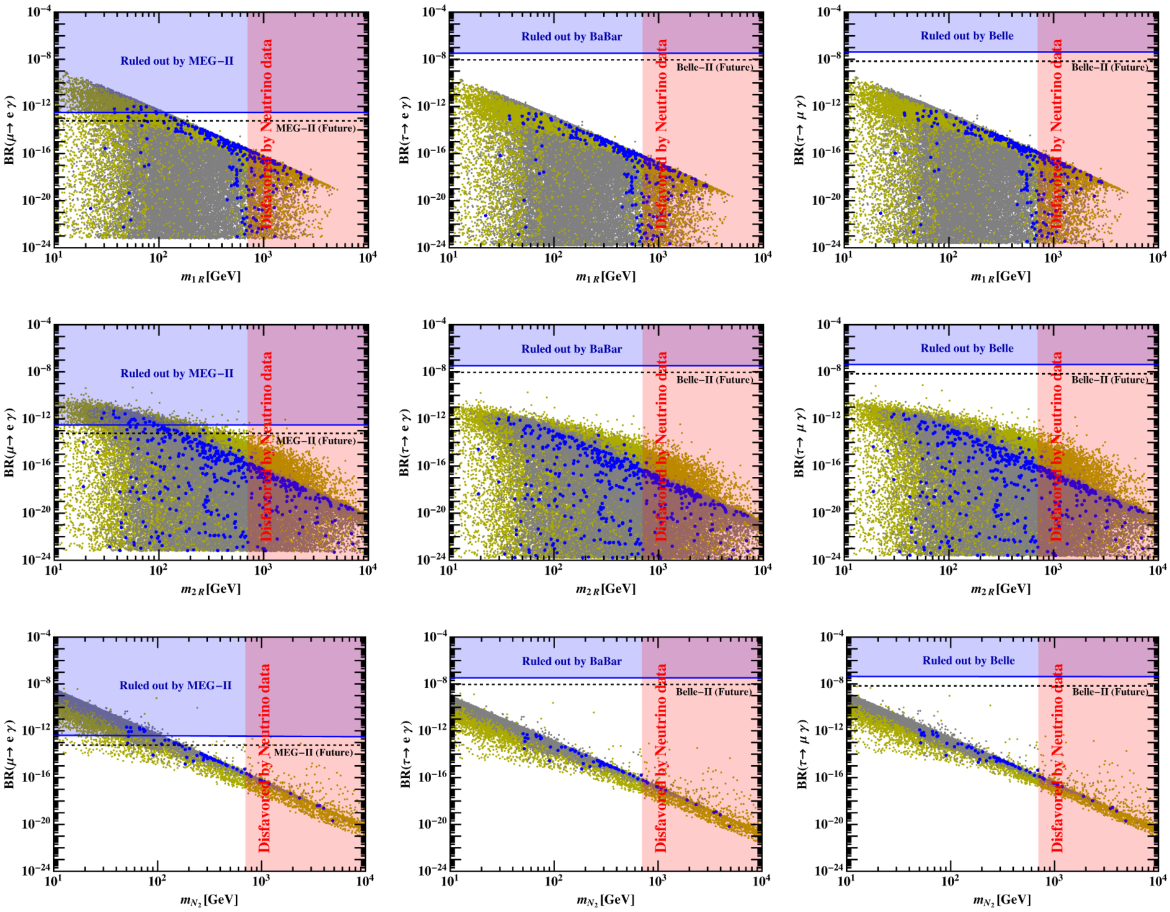

Figure 12. The CLFV rates vs DM mass have been shown. *1st column:* BR($\mu \to e\gamma$), *2nd column:* BR($\tau \to e\gamma$), *3rd column:* BR($\tau \to \mu\gamma$). *1st row:* doublet scalar DM mass, *2nd row:* singlet scalar DM mass, *3rd row:* fermionic DM mass. The gray and olive green points represent regions of under-abundance and over-abundance, respectively, while the blue points correspond to the correct relic density.

relic density. Note that all three processes show similar behavior: their maximum values drop as the DM mass increases. This behavior arises because DM is the lightest particle in the dark sector. As its mass increases, the other dark sector particles also become heavier, which lowers the CLFV rates, as can be seen from eq. (5.1). In our analysis, we identified viable data points in the mass ranges of (63–150) GeV for the doublet scalar, (48–265) GeV for the singlet scalar, and (50–160) GeV for the fermionic DM candidate, all of which satisfy the previously discussed experimental constraints. Notably, these points lie between the current experimental bounds and the projected future sensitivity for the decay $\mu \to e\gamma$. However, for the decay channels $\tau \to e\gamma$ and $\tau \to \mu\gamma$, no points within our scanned parameter space fall within the current or expected experimental limits. This is primarily due to the comparatively weaker experimental bounds for these decay modes, which our model does not reach within the explored parameter range. Thus, CLFV points that are both within experimental reach and consistent with DM constraints appear only in a few distinct regions, making CLFV measurements a valuable probe for testing our model.

JHEP10(2025)088

6 Conclusions

We propose a Dirac scotogenic-like model where DM stability arises from the breaking of an A_4 flavor symmetry. The same breaking also induces a "scoto inverse-seesaw" mechanism, which combines a tree-level inverse-seesaw with a one-loop scotogenic contribution to generate neutrino masses. The inverse seesaw mechanism at the tree level is enabled by the smallness of the singlet VEV u. This framework naturally explains the observed neutrino mass-squared differences, Δm^2_{atm} and Δm^2_{sol}, from oscillation data. The model also addresses leptonic flavor patterns via the A_4 symmetry. It includes right-handed neutrinos ν_R, $\text{SU}(2)_L$ singlet fermions N_L, N_R, a singlet scalar ξ, and a doublet scalar η. Here, ν_R's are A_4 singlets, while all other BSM particles transform as A_4 triplets. To forbid tree-level neutrino couplings before symmetry breaking, we assign specific $B-L$ charges $(-4,-4,5)$ to ν_R. The breaking $\text{U}(1)_{B-L} \to \mathcal{Z}_3$ then ensures neutrinos remain Dirac in nature and results in one massless neutrino.

Our model is compatible with both normal (NO) and inverted (IO) neutrino mass orderings. In both cases, we find a strong correlation between the sum of neutrino masses $\sum m_i$ and the effective beta decay mass $\langle m_\beta \rangle$, with both quantities confined within narrow ranges. For the IO scenario, neutrino masses exhibit particularly sharp correlations (see right panel of figure 6). We also examine the correlation between the CP-violating phase δ_{CP} and the atmospheric mixing angle θ_{23} for two benchmark scenarios. For NO, case-I aligns more closely with the global best-fit value, whereas case-II remains consistent within the 2σ range. For IO, both scenarios allow a broader range of δ_{CP} values, still compatible with the best-fit value. These predictions provide testable signatures that can be probed in upcoming neutrino oscillation experiments.

Constraints from neutrino oscillation data impose an upper bound on the VEV of the singlet scalar u, which in turn limits scalar masses due to the requirement of perturbative Yukawa couplings. These theoretical bounds significantly influence dark sector predictions, restricting the DM mass to an upper limit of ~ 700 GeV. Incorporating collider (LHC and LEP) and DD constraints further narrows the viable DM parameter space. For doublet scalar DM, the allowed mass range is $85 \leq m_{1R} \leq 700$ GeV, though the lower region is nearly ruled out by DD bounds. Singlet scalar DM remains viable in the $20 \leq m_{2R} \leq 700$ GeV range. Fermionic DM remains viable in the mass range $10 \leq M_{N_2} \leq 700$ GeV. Thus, the model predicts DM candidates with masses confined to narrow, experimentally and theoretically motivated windows.

We have also analyzed lepton LFV decays, such as $\mu \to e\gamma$, for the three DM candidates in our model. By comparing the predicted branching ratios with current limits from MEG, BaBar, and Belle, as well as projected future sensitivities, we find that viable regions of parameter space remain consistent with all LFV constraints. Overall, the flavor symmetry-breaking framework not only ensures the stability of DM but also leads to a novel *scoto inverse-seesaw* mechanism. This yields a unified and predictive framework for both neutrino mass generation and DM phenomenology. As a result, the model offers tightly constrained and testable predictions in both the neutrino and dark sectors, potentially verifiable in upcoming experimental efforts.

JHEP10(2025)088

Acknowledgments

Authors would like to acknowledge the SARAH-4.14.5 [58] and SPheno-4.0.5 [59] to compute all vertex diagrams, mass matrices, and tadpole equations. Additionally, the thermal contribution to the DM relic density, as well as the cross sections for DM-nucleon scattering, are evaluated using micrOMEGAs-5.3.41 [60]. RK and SY would like to acknowledge the funding support by the CSIR SRF-NET fellowship.

A Scalar potential and mass spectrum

In the scalar sector, the $\mathrm{SU}(2)_L$ doublet H is a singlet under the A_4 symmetry, while the doublet η and the singlet ξ transform as triplets. The potential is formulated based on the specified $\mathrm{SU(2)_L \otimes U(1)_Y}$ and A_4 charge assignment for the scalar fields

$$V = V_H + V_\eta + V_\xi + V_{H\eta} + V_{H\xi} + V_{\eta\xi} + V_{H\eta\xi} + \text{h.c.}\,. \tag{A.1}$$

The individual terms in the potential are explicitly written as:

$$\begin{aligned}
V_H =& \mu_H^2 H^\dagger H + \lambda_1 (H^\dagger H)^2,\\
V_\eta =& \mu_\eta^2 (\eta^\dagger\eta)_{\mathbf{1}} + \lambda_{\eta_1}(\eta^\dagger\eta)_{\mathbf{1}}(\eta^\dagger\eta)_{\mathbf{1}} + \lambda_{\eta_2}(\eta^\dagger\eta)_{\mathbf{1'}}(\eta^\dagger\eta)_{\mathbf{1''}} + \lambda_{\eta_3}(\eta^\dagger\eta^\dagger)_{\mathbf{1}}(\eta\eta)_{\mathbf{1}} + \lambda_{\eta_4}(\eta^\dagger\eta^\dagger)_{\mathbf{1'}}(\eta\eta)_{\mathbf{1''}}\\
&+\lambda_{\eta_5}(\eta^\dagger\eta^\dagger)_{\mathbf{1''}}(\eta\eta)_{\mathbf{1'}} + \lambda_{\eta_6}(\eta^\dagger\eta)_{\mathbf{3_1}}(\eta^\dagger\eta)_{\mathbf{3_1}} + \lambda_{\eta_7}(\eta^\dagger\eta)_{\mathbf{3_1}}(\eta^\dagger\eta)_{\mathbf{3_2}} + \lambda_{\eta_8}(\eta^\dagger\eta)_{\mathbf{3_2}}(\eta^\dagger\eta)_{\mathbf{3_2}}\\
&+\lambda_{\eta_9}(\eta^\dagger\eta^\dagger)_{\mathbf{3_1}}(\eta\eta)_{\mathbf{3_1}} + \lambda_{\eta_{10}}(\eta^\dagger\eta^\dagger)_{\mathbf{3_1}}(\eta\eta)_{\mathbf{3_2}} + \lambda_{\eta_{11}}(\eta^\dagger\eta^\dagger)_{\mathbf{3_2}}(\eta\eta)_{\mathbf{3_1}} + \lambda_{\eta_{12}}(\eta^\dagger\eta^\dagger)_{\mathbf{3_2}}(\eta\eta)_{\mathbf{3_2}},\\
V_\xi =& \mu_\xi^2(\xi\xi)_{\mathbf{1}} + \lambda_{\xi_1}(\xi\xi)_{\mathbf{1}}(\xi\xi)_{\mathbf{1}} + \lambda_{\xi_2}(\xi\xi)_{\mathbf{1'}}(\xi\xi)_{\mathbf{1''}} + \lambda_{\xi_3}(\xi\xi)_{\mathbf{3_1}}(\xi\xi)_{\mathbf{3_1}} + \lambda_{\xi_4}(\xi\xi)_{\mathbf{3_1}}(\xi\xi)_{\mathbf{3_2}}\\
&+\lambda_{\xi_5}(\xi\xi)_{\mathbf{3_2}}(\xi\xi)_{\mathbf{3_2}},\\
V_{H\eta} =& \lambda_{H\eta_1}(H^\dagger H)(\eta^\dagger\eta)_{\mathbf{1}} + \lambda_{H\eta_2}(H^\dagger\eta)_{\mathbf{3}}(\eta^\dagger H)_{\mathbf{3}} + \lambda_{H\eta_3}(H^\dagger\eta^\dagger)_{\mathbf{3}}(\eta H)_{\mathbf{3}},\\
V_{H\xi} =& \lambda_{H\xi_1}(H^\dagger H)(\xi\xi)_{\mathbf{1}} + \lambda_{H\xi_2}(H^\dagger\xi)_{\mathbf{3}}(\xi H)_{\mathbf{3}},\\
V_{\eta\xi} =& [\lambda_{\eta\xi_1}(\eta^\dagger\eta)_{\mathbf{1}}(\xi\xi)_{\mathbf{1}} + \lambda_{\eta\xi_2}(\eta^\dagger\eta)_{\mathbf{1'}}(\xi\xi)_{\mathbf{1''}} + \lambda_{\eta\xi_3}(\eta^\dagger\eta)_{\mathbf{1''}}(\xi\xi)_{\mathbf{1'}}]\\
&+[\lambda_{\eta\xi_4}(\eta^\dagger\eta)_{\mathbf{3_1}}(\xi\xi)_{\mathbf{3_1}} + \lambda_{\eta\xi_5}(\eta^\dagger\eta)_{\mathbf{3_1}}(\xi\xi)_{\mathbf{3_2}} + \lambda_{\eta\xi6}(\eta^\dagger\eta)_{\mathbf{3_2}}(\xi\xi)_{\mathbf{3_1}} + \lambda_{\eta\xi7}(\eta^\dagger\eta)_{\mathbf{3_2}}(\xi\xi)_{\mathbf{3_2}}]\\
&+[\lambda_{\eta\xi_8}(\eta^\dagger\xi)_{\mathbf{1}}(\eta\xi)_{\mathbf{1}} + \lambda_{\eta\xi_9}(\eta^\dagger\xi)_{\mathbf{1'}}(\eta\xi)_{\mathbf{1''}} + \lambda_{\eta\xi_{10}}(\eta^\dagger\xi)_{\mathbf{1''}}(\eta\xi)_{\mathbf{1'}}]\\
&+[\lambda_{\eta\xi_{11}}(\eta^\dagger\xi)_{\mathbf{3_1}}(\eta\xi)_{\mathbf{3_1}} + \lambda_{\eta\xi_{12}}(\eta^\dagger\xi)_{\mathbf{3_1}}(\eta\xi)_{\mathbf{3_2}} + \lambda_{\eta\xi_{13}}(\eta^\dagger\xi)_{\mathbf{3_2}}(\eta\xi)_{\mathbf{3_1}} + \lambda_{\eta\xi_{14}}(\eta^\dagger\xi)_{\mathbf{3_2}}(\eta\xi)_{\mathbf{3_2}}],\\
V_{H\eta\xi} =& \kappa(H^\dagger)_{\mathbf{1}}(\eta\xi)_{\mathbf{1}} + \text{h.c.}
\end{aligned} \tag{A.2}$$

Now, following the A_4 multiplication rule as given in eqs. (B.2) and (B.4), the expressions given in eq. (A.2) can be simplified in the component form as

$$\begin{aligned}
V_H =& \mu_H^2 H^\dagger H + \lambda_1 (H^\dagger H)^2,\\
V_\eta =& \mu_\eta^2(\eta_1^\dagger\eta_1 + \eta_2^\dagger\eta_2 + \eta_3^\dagger\eta_3) + (\lambda_{\eta_1} + \lambda_{\eta_2} + \lambda_{\eta_3} + 2\lambda_{\eta_4})(\eta_1^\dagger\eta_1\eta_1^\dagger\eta_1 + \eta_2^\dagger\eta_2\eta_2^\dagger\eta_2 + \eta_3^\dagger\eta_3\eta_3^\dagger\eta_3)\\
&+(2\lambda_{\eta_1} - \lambda_{\eta_2} + \lambda_{\eta_{10}} + \lambda_{\eta_{11}})(\eta_1^\dagger\eta_1\eta_2^\dagger\eta_2 + \eta_1^\dagger\eta_1\eta_3^\dagger\eta_3 + \eta_2^\dagger\eta_2\eta_3^\dagger\eta_3)\\
&+(\lambda_{\eta_3} - \lambda_{\eta_4} + \lambda_{\eta_6})(\eta_2^\dagger\eta_3\eta_2^\dagger\eta_3 + \eta_3^\dagger\eta_1\eta_3^\dagger\eta_1 + \eta_1^\dagger\eta_2\eta_1^\dagger\eta_2 + \text{h.c.})\\
&+(\lambda_{\eta_7} + \lambda_{\eta_9} + \lambda_{\eta_{12}})(\eta_2^\dagger\eta_3\eta_3^\dagger\eta_2 + \eta_3^\dagger\eta_1\eta_1^\dagger\eta_3 + \eta_1^\dagger\eta_2\eta_2^\dagger\eta_1),
\end{aligned}$$

JHEP10(2025)088

$$
\begin{aligned}
V_\xi = & \mu_\xi^2(\xi_1\xi_1+\xi_2\xi_2+\xi_3\xi_3)+(\lambda_{\xi_1}+\lambda_{\xi_2})(\xi_1\xi_1\xi_1\xi_1+\xi_2\xi_2\xi_2\xi_2+\xi_3\xi_3\xi_3\xi_3) \\
& +(2\lambda_{\xi_1}-\lambda_{\xi_2}+\lambda_{\xi_3}+\lambda_{\xi_4}+\lambda_{\xi_5})(\xi_1\xi_1\xi_2\xi_2+\xi_1\xi_1\xi_3\xi_3+\xi_2\xi_2\xi_3\xi_3), \\
V_{H\eta} = & (\lambda_{H\eta_1}+\lambda_{H\eta_3})(H^\dagger H\eta_1^\dagger\eta_1+H^\dagger H\eta_2^\dagger\eta_2+H^\dagger H\eta_3^\dagger\eta_3) \\
& +\lambda_{H\eta_2}(H^\dagger\eta_1\eta_1^\dagger H+H^\dagger\eta_2\eta_2^\dagger H+H^\dagger\eta_3\eta_3^\dagger H), \\
V_{H\xi} = & (\lambda_{H\xi_1}+\lambda_{H\xi_2})\left(H^\dagger H\xi_1\xi_1+H^\dagger H\xi_2\xi_2+H^\dagger H\xi_3\xi_3\right), \\
V_{\eta\xi} = & (\lambda_{\eta\xi_1}+2\lambda_{\eta\xi_2}+\lambda_{\eta\xi_8}+2\lambda_{\eta\xi_9})(\eta_1^\dagger\eta_1\xi_1\xi_1+\eta_2^\dagger\eta_2\xi_2\xi_2+\eta_3^\dagger\eta_3\xi_3\xi_3) \\
& +(\lambda_{\eta\xi_4}+\lambda_{\eta\xi_5}+\lambda_{\eta\xi_{12}}+\lambda_{\eta\xi_8}-\lambda_{\eta\xi_9})(\eta_2^\dagger\eta_3\xi_2\xi_3+\eta_3^\dagger\eta_1\xi_3\xi_1+\eta_1^\dagger\eta_2\xi_1\xi_2+\text{h.c.}) \\
& +(\lambda_{\eta\xi_1}-\lambda_{\eta\xi_2}+\lambda_{\eta\xi_{11}})(\eta_2^\dagger\xi_3\eta_2\xi_3+\eta_3^\dagger\xi_1\eta_3\xi_1+\eta_1^\dagger\xi_2\eta_1\xi_2) \\
& +(\lambda_{\eta\xi_1}-\lambda_{\eta\xi_2}+\lambda_{\eta\xi_{14}})(\eta_3^\dagger\xi_2\eta_3\xi_2+\eta_1^\dagger\xi_3\eta_1\xi_3+\eta_2^\dagger\xi_1\eta_2\xi_1), \\
V_{H\eta\xi} = & \kappa(H^\dagger\eta_1\xi_1+H^\dagger\eta_2\xi_2+H^\dagger\eta_3\xi_3)+\text{h.c.}.
\end{aligned}
\tag{A.3}
$$

We can now compute the scalar mass spectrum of the model. The particles in the model are classified as $\mathcal{Z}_2$ even or $\mathcal{Z}_2$ odd, on their transformation properties under A_4. Since the $\mathcal{Z}_2$ symmetry remains unbroken, only $\mathcal{Z}_2$ even particles mix among themselves, and similarly, $\mathcal{Z}_2$ odd particles mix only with each other. The $\mathcal{Z}_2$ even particles (ϕ_1,ϕ_2,ϕ_3) mix with each other giving $\mathcal{M}_H^2$ matrix. Similarly, the $\mathcal{Z}_2$ even particles (σ_1,σ_2) mix to give the mass matrix $\mathcal{M}_A^2$, while $(H^\pm,\eta_1^\pm)$ mix to form the mass matrix $\mathcal{M}_{H^\pm}^2$. The $\mathcal{Z}_2$ odd particles (η_2^R,ξ_2^R) and (η_3^R,ξ_3^R) do mix as well as $(\eta_2^\pm,\eta_3^\pm)$ among themselves giving $\mathcal{M}_2^2$, $\mathcal{M}_3^2$ and $\mathcal{M}^2_{\eta^\pm_{2/3}}$ mass matrices, respectively.

These matrices are as follows:

$$
\mathcal{M}_H^2=\begin{bmatrix} 2\lambda_1 v_1^2-\frac{\kappa v_2 u}{v_1} & \Lambda_{12}v_1v_2+\kappa u & \kappa v_2+2\lambda_{H\xi_1}+\lambda_{H\xi_2}v_1u \\ \Lambda_{12}v_1v_2+\kappa u & 2\Lambda_\eta v_2^2-\frac{\kappa v_1 u}{v_2} & 2\Lambda_{23}v_2u+\kappa v_1 \\ \kappa v_2+2\lambda_{H\xi_1}+\lambda_{H\xi_2}v_1u & 2\Lambda_{23}v_2u+\kappa v_1 & 8\Lambda_\xi u^2-\frac{\kappa v_1 v_2}{u}\end{bmatrix},
$$

$$
\mathcal{M}_A^2=\begin{bmatrix}-\frac{\kappa v_2 u}{v_1} & \kappa u \\ \kappa u & -\frac{\kappa v_1 u}{v_2}\end{bmatrix},\ \mathcal{M}_{H^\pm}^2=\begin{bmatrix}-\left(\frac{\lambda_{H\eta_2}}{2}v_2^2+\frac{\kappa v_2 u}{v_1}\right) & \frac{\lambda_{H\eta_2}}{2}v_1v_2+\kappa u \\ \frac{\lambda_{H\eta_2}}{2}v_1v_2+\kappa u & -\left(\frac{\lambda_{H\eta_2}}{2}v_2^2+\frac{\kappa v_1 u}{v_2}\right)\end{bmatrix},
$$

$$
\mathcal{M}_{2R}^2=\begin{bmatrix}\Lambda_{\eta_2}v_2^2-\alpha_2u^2 & \alpha_1v_2u \\ \alpha_1v_2u & \Lambda_{\xi_2}u^2-\alpha_3v_2^2\end{bmatrix},\ \mathcal{M}_{3R}^2=\begin{bmatrix}\Lambda_{\eta_2}v_2^2-\alpha_3u^2 & \alpha_1v_2u \\ \alpha_1v_2u & \Lambda_{\xi_2}u^2-\alpha_2v_2^2\end{bmatrix},
$$

$$
\mathcal{M}^2_{\eta^\pm_{2/3}}=\begin{bmatrix}m_2^\pm & 0 \\ 0 & m_3^\pm\end{bmatrix},\quad \mathcal{M}^2_{\eta^I_{2/3}}=\begin{bmatrix}m_2^I & 0 \\ 0 & m_3^I\end{bmatrix}, \tag{A.4}
$$

where

$$
\begin{aligned}
m_2^\pm &= -\frac{\lambda_{H\eta_2}}{2}v_1^2-\left(\frac{3}{2}\lambda_{\eta_2}+\lambda_{\eta_3}+2\lambda_{\eta_4}-\frac{1}{2}\lambda_{\eta_{10}}+\lambda_{\eta_{11}}\right)v_2^2-\alpha_2u^2, \\
m_3^\pm &= -\frac{\lambda_{H\eta_2}}{2}v_1^2-\left(\frac{3}{2}\lambda_{\eta_2}+\lambda_{\eta_3}+2\lambda_{\eta_4}-\frac{1}{2}\lambda_{\eta_{10}}+\lambda_{\eta_{11}}\right)v_2^2-\alpha_3u^2, \\
m_2^I &= (-3\lambda_{\eta_2}+\lambda_{\eta_{10}}+\lambda_{\eta_{11}}+\lambda_{\eta_7}+\lambda_{\eta_9}+\lambda_{\eta_{12}}-4\lambda_{\eta_3}-2\lambda_{\eta_4}-2\lambda_{\eta_6})\frac{v_2^2}{2} \\
& \quad -\kappa\frac{v_1u}{v_2}+(\lambda_{\eta\xi_{14}}-3\lambda_{\eta\xi_2}-\lambda_{\eta\xi_8}-2\lambda_{\eta\xi_9})v_3^2,
\end{aligned}
$$

$$m_3^I = (-3\lambda_{\eta_2} + \lambda_{\eta_{10}} + \lambda_{\eta_{11}} + \lambda_{\eta_7} + \lambda_{\eta_9} + \lambda_{\eta_{12}} - 4\lambda_{\eta_3} - 2\lambda_{\eta_4} - 2\lambda_{\eta_6})\,\frac{v_2^2}{2} - \kappa\frac{v_1 u}{v_2} + (\lambda_{\eta\xi_{11}} - 3\lambda_{\eta\xi_2} - \lambda_{\eta\xi_8} - 2\lambda_{\eta\xi_9})\, v_3^2.$$

The following combinations of couplings have been used in above mass matrices

$$\begin{aligned}
&\Lambda_\eta \equiv \lambda_{\eta_1} + \lambda_{\eta_2} + \lambda_{\eta_3} + 2\lambda_{\eta_4}, \qquad \Lambda_\xi \equiv \lambda_{\xi_1} + \lambda_{\xi_2},\\
&\alpha_2 \equiv \frac{\kappa v_1}{v_2 u} + (3\lambda_{\eta\xi_2} + \lambda_{\eta\xi_8} + 2\lambda_{\eta\xi_9} - \lambda_{\eta\xi_{14}}), \qquad \alpha_1 \equiv \frac{\kappa v_1}{v_2 u} + \lambda_{\eta\xi_4} + \lambda_{\eta\xi_5} + \lambda_{\eta\xi_{12}} + \lambda_{\eta\xi_8} - \lambda_{\eta\xi_9},\\
&\Lambda_{12} \equiv \lambda_{H\eta_2} + \lambda_{H\eta_4}, \qquad \Lambda_{23} \equiv \lambda_{\eta\xi_1} + 2\lambda_{\eta\xi_2} + \lambda_{\eta\xi_8} + 2\lambda_{\eta\xi_9},\\
&\Lambda_{\eta_2} \equiv \lambda_{\eta_6} - \frac{3}{2}\lambda_{\eta_2} - 3\lambda_{\eta_4} + \frac{1}{2}\lambda_{\eta_{10}} + \lambda_{\eta_{11}} + \frac{1}{2}\lambda_{\eta_7} + \lambda_{\eta_9} + \lambda_{\eta_{12}}, \qquad \Lambda_3 \equiv \lambda_{\xi_3} + \frac{1}{2}\lambda_{\xi_4} - \frac{3}{2}\lambda_{\xi_2}.\\
&\Lambda_{\xi_2} \equiv 2\lambda_{\xi_3} + \lambda_{\xi_4} + \lambda_{\xi_5} - 6\lambda_{\xi_2}, \qquad \alpha_3 \equiv \frac{\kappa v_1}{v_2 u} + (3\lambda_{\eta\xi_2} + \lambda_{\eta\xi_8} + 2\lambda_{\eta\xi_9} - \lambda_{\eta\xi_{11}}).
\end{aligned} \tag{A.5}$$

B A_4 symmetry and its multiplication rule

The A_4 symmetry is a non-abelian discrete flavor group, corresponding to the even permutation group of four objects. This symmetry is also the group of symmetries for a regular tetrahedron. With its 12 elements, A_4 can be generated by two generators, denoted as S and T, which satisfy the following relations

$$S^2 = T^3 = (ST)^3 = \mathcal{I}. \tag{B.1}$$

A_4 symmetry group features four distinct irreducible representations: one triplet, denoted as 3, and three singlets, labeled as 1, $1'$, and $1''$. Their multiplication rules are as follows:

$$\begin{aligned}
&1 \times 1 = 1 = 1' \times 1'', \quad 1' \times 1' = 1'', \quad 1'' \times 1'' = 1',\\
&1 \times 3 = 3, \quad 3 \times 3 = 1 + 1' + 1'' + 3_1 + 3_2\,.
\end{aligned} \tag{B.2}$$

In the basis where generators S and T are real matrices, they are given by

$$S = \begin{pmatrix} 1 & 0 & 0 \\ 0 & -1 & 0 \\ 0 & 0 & -1 \end{pmatrix}, \quad T = \begin{pmatrix} 0 & 1 & 0 \\ 0 & 0 & 1 \\ 1 & 0 & 0 \end{pmatrix}. \tag{B.3}$$

If $a = (a_1, a_2, a_3)$ and $b = (b_1, b_2, b_3)$ are two triplets of A_4, then they obey the following multiplication rules [33, 61]

$$\begin{aligned}
(ab)_1 &= a_1 b_1 + a_2 b_2 + a_3 b_3\,,\\
(ab)_{1'} &= a_1 b_1 + \omega a_2 b_2 + \omega^2 a_3 b_3\,,\\
(ab)_{1''} &= a_1 b_1 + \omega^2 a_2 b_2 + \omega a_3 b_3\,,\\
(ab)_{3_1} &= (a_2 b_3, a_3 b_1, a_1 b_2)\,,\\
(ab)_{3_2} &= (a_3 b_2, a_1 b_3, a_2 b_1)\,.
\end{aligned} \tag{B.4}$$

Here, $\omega^3 = 1$, denotes a cube root of unity. The generator S remains invariant under VEV alignments $\langle\varphi\rangle \sim (v, 0, 0)$, which leads to the breaking of the A_4 symmetry into its subgroup $\mathcal{Z}_2$.

$$S\langle\varphi\rangle = \langle\varphi\rangle. \tag{B.5}$$

For a A_4 triplet, any field $\psi \equiv (a_1, a_2, a_3)^T$ transforms under S as follows

$$S\psi = \begin{pmatrix} 1 & 0 & 0 \\ 0 & -1 & 0 \\ 0 & 0 & -1 \end{pmatrix} \begin{pmatrix} a_1 \\ a_2 \\ a_3 \end{pmatrix} = \begin{pmatrix} a_1 \\ -a_2 \\ -a_3 \end{pmatrix} \tag{B.6}$$

Once A_4 symmetry is broken, the $\mathcal{Z}_2$ residual symmetry for triplets N, η and ξ is given as

$$\begin{aligned} N_1 &\to +N_1\,, \quad \eta_1 \to +\eta_1\,, \quad \xi_1 \to +\xi_1\,, \\ N_{2,3} &\to -N_{2,3}\,, \quad \eta_{2,3} \to -\eta_{2,3}\,, \quad \eta_{2,3} \to -\eta_{2,3}\,. \end{aligned} \tag{B.7}$$

The remaining fields of our model are $\mathcal{Z}_2$ even, because they are singlets of A_4 and transform trivially under S.

C Annihilation, production and detection of DM

In this section, we present the possible Feynman diagrams that play an important role in determining the relic density of different DM candidates, doublet and singlet scalar, as well as fermion. In addition, we include Feynman diagrams for DD, for scalars at tree level, and for fermionic DM at loop level. These Feynman diagrams serve to assist our understanding of the dark sector results presented in section 4.

JHEP10(2025)088

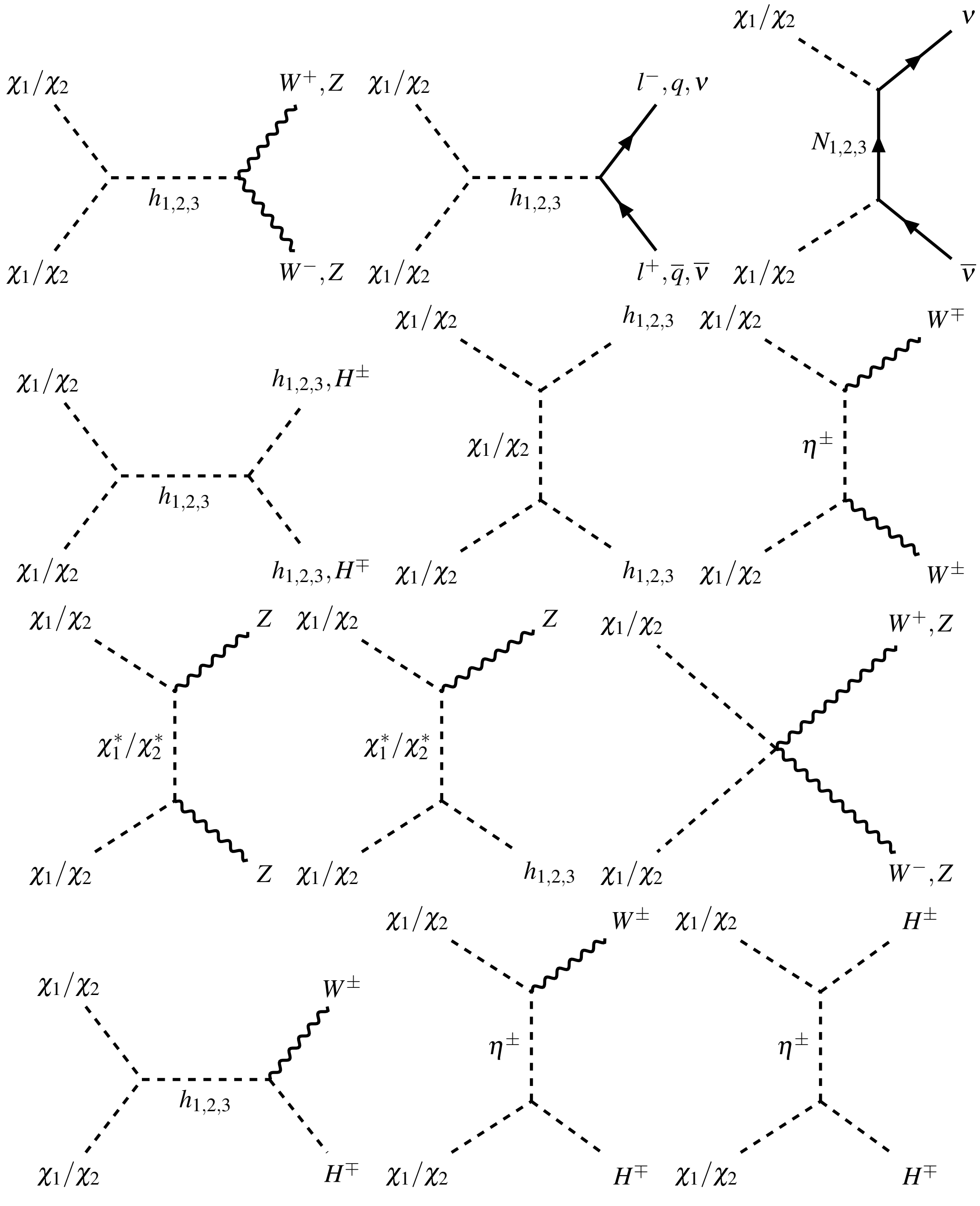

Figure 13. Relevant diagrams for the computation of relic density of the scalar DM candidate (*continues …*)

JHEP10(2025)088

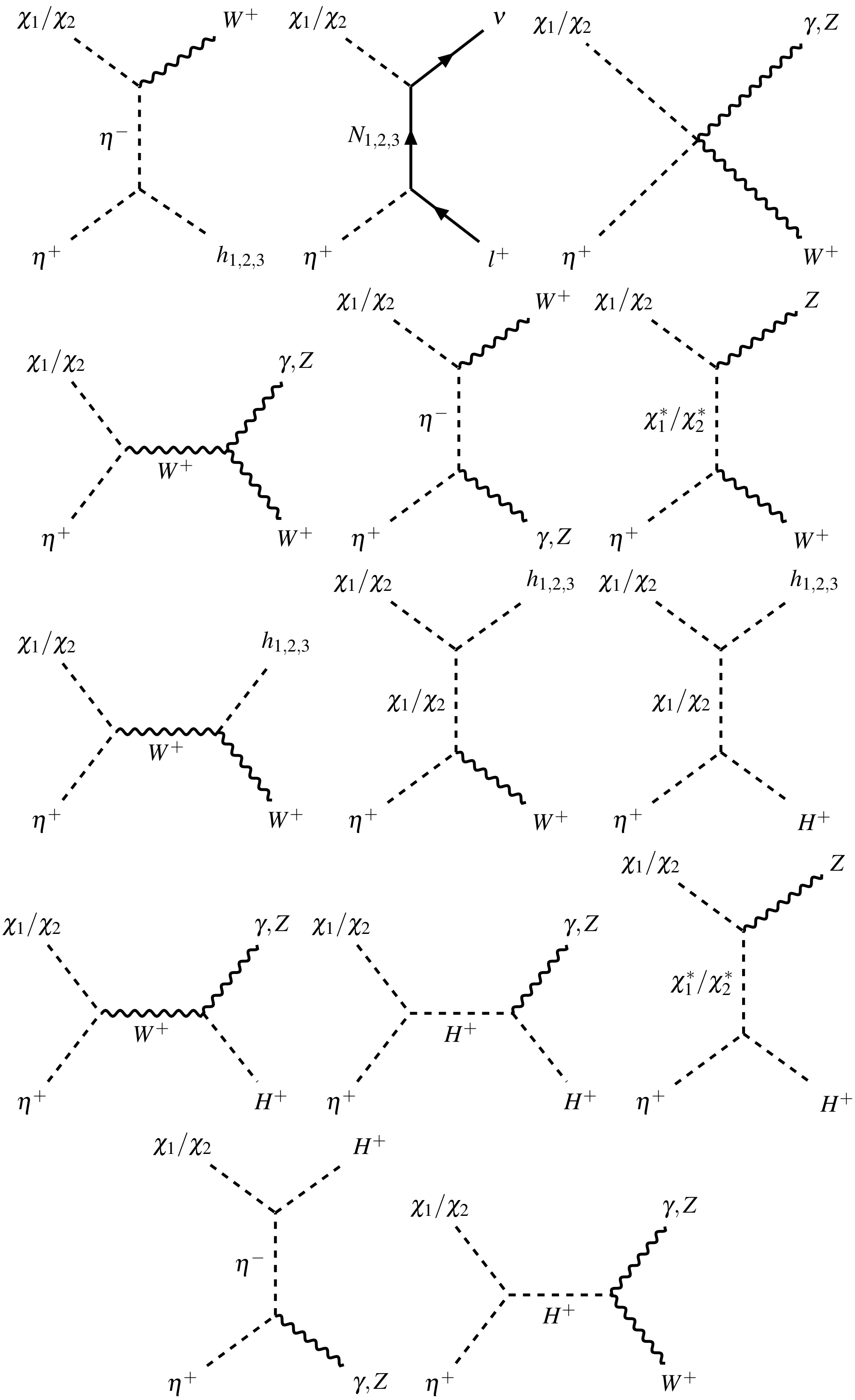

Figure 13. Relevant diagrams for the computation of relic density of the scalar DM candidate (*continues ...*).

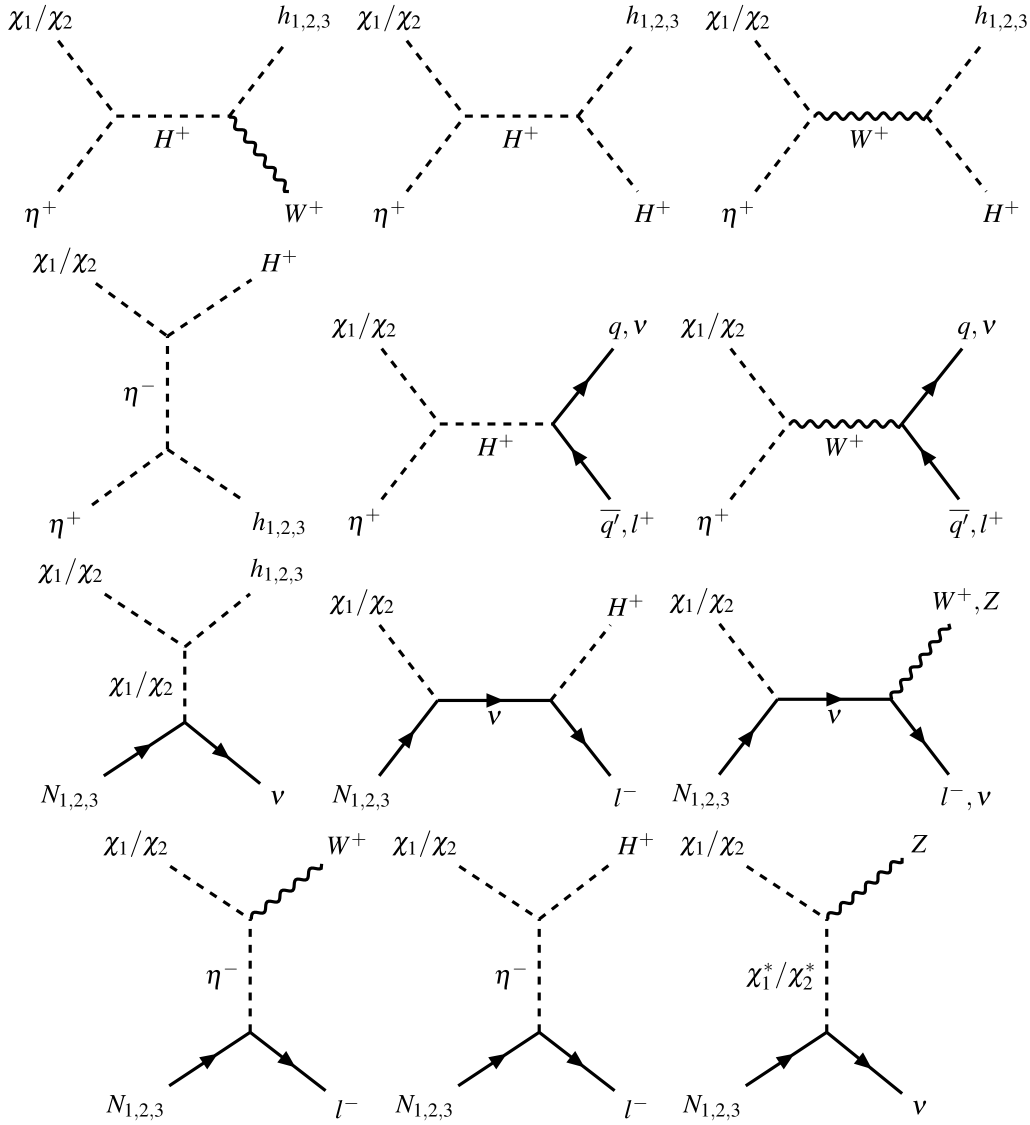

Figure 13. Relevant diagrams for the computation of relic density of the scalar DM candidate.

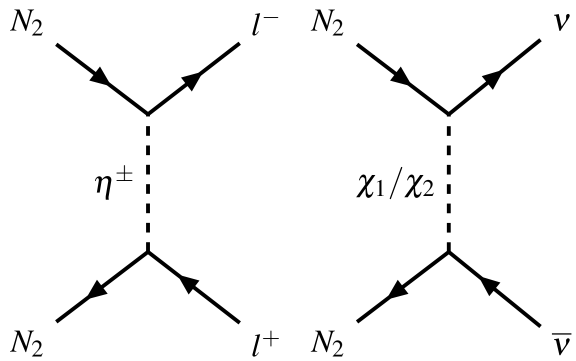

Figure 14. Relevant diagrams for the computation of relic density of the fermion DM candidate.

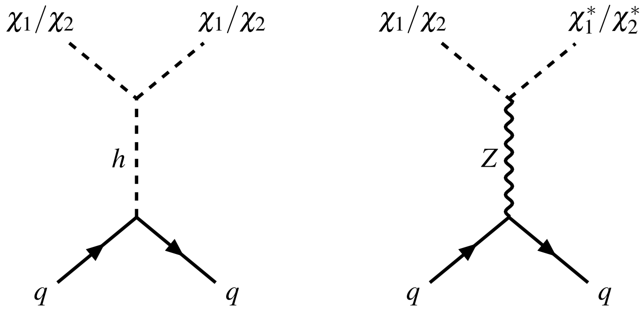

Figure 15. Relevant diagrams for the direct detection of the scalar DM candidate.

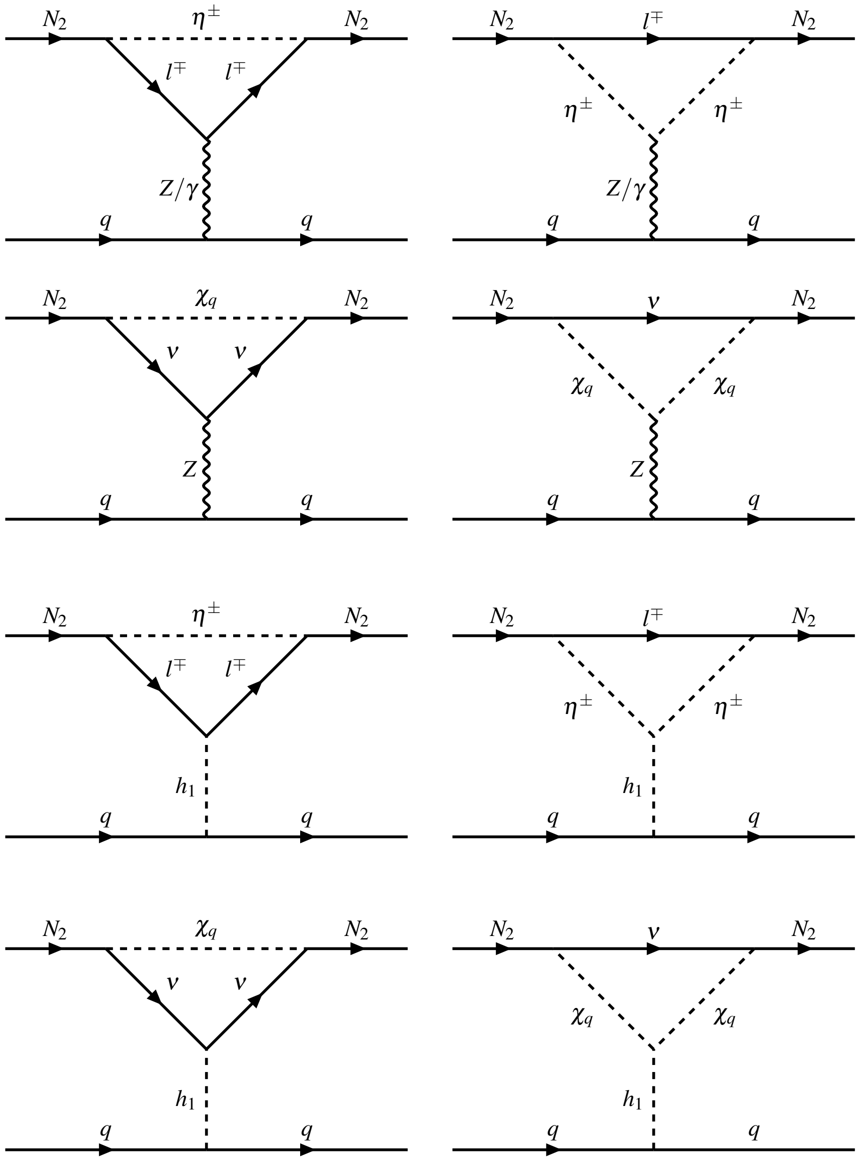

Figure 16. Relevant diagrams for the direct detection of the fermion DM candidate.

Data Availability Statement. This article has no associated data or the data will not be deposited.

Code Availability Statement. This article has no associated code or the code will not be deposited.

References

[1] SNO collaboration, *Measurement of the rate of $\nu_e + d \to p + p + e^-$ interactions produced by ^8B solar neutrinos at the Sudbury Neutrino Observatory*, *Phys. Rev. Lett.* **87** (2001) 071301 [nucl-ex/0106015] [INSPIRE].

[2] Super-Kamiokande collaboration, *Evidence for oscillation of atmospheric neutrinos*, *Phys. Rev. Lett.* **81** (1998) 1562 [hep-ex/9807003] [INSPIRE].

[3] Planck collaboration, *Planck 2018 results. VI. Cosmological parameters*, *Astron. Astrophys.* **641** (2020) A6 [*Erratum ibid.* **652** (2021) C4] [arXiv:1807.06209] [INSPIRE].

[4] E. Ma, *Verifiable radiative seesaw mechanism of neutrino mass and dark matter*, *Phys. Rev. D* **73** (2006) 077301 [hep-ph/0601225] [INSPIRE].

[5] F. Capozzi et al., *Unfinished fabric of the three neutrino paradigm*, *Phys. Rev. D* **104** (2021) 083031 [arXiv:2107.00532] [INSPIRE].

[6] P.F. de Salas et al., *2020 global reassessment of the neutrino oscillation picture*, *JHEP* **02** (2021) 071 [arXiv:2006.11237] [INSPIRE].

[7] I. Esteban et al., *The fate of hints: updated global analysis of three-flavor neutrino oscillations*, *JHEP* **09** (2020) 178 [arXiv:2007.14792] [INSPIRE].

[8] N. Rojas, R. Srivastava and J.W.F. Valle, *Simplest Scoto-Seesaw Mechanism*, *Phys. Lett. B* **789** (2019) 132 [arXiv:1807.11447] [INSPIRE].

[9] D.M. Barreiros, F.R. Joaquim, R. Srivastava and J.W.F. Valle, *Minimal scoto-seesaw mechanism with spontaneous CP violation*, *JHEP* **04** (2021) 249 [arXiv:2012.05189] [INSPIRE].

[10] S. Mandal, R. Srivastava and J.W.F. Valle, *The simplest scoto-seesaw model: WIMP dark matter phenomenology and Higgs vacuum stability*, *Phys. Lett. B* **819** (2021) 136458 [arXiv:2104.13401] [INSPIRE].

[11] D.M. Barreiros, H.B. Camara and F.R. Joaquim, *Flavour and dark matter in a scoto/type-II seesaw model*, *JHEP* **08** (2022) 030 [arXiv:2204.13605] [INSPIRE].

[12] J. Ganguly, J. Gluza, B. Karmakar and S. Mahapatra, *Phenomenology of the flavor symmetric scoto-seesaw model with dark matter and TM1 mixing*, *Phys. Rev. D* **110** (2024) 035012 [arXiv:2311.15997] [INSPIRE].

[13] J. Ganguly, J. Gluza and B. Karmakar, *Common origin of θ_{13} and dark matter within the flavor symmetric scoto-seesaw framework*, *JHEP* **11** (2022) 074 [arXiv:2209.08610] [INSPIRE].

[14] P. Van Dong and D. Van Loi, *Scotoseesaw model implied by dark right-handed neutrinos*, *Phys. Rev. D* **110** (2024) 115022 [arXiv:2311.09795] [INSPIRE].

JHEP10(2025)088

[15] J. Leite, S. Sadhukhan and J.W.F. Valle, *Dynamical scoto-seesaw mechanism with gauged B-L symmetry*, *Phys. Rev. D* **109** (2024) 035023 [arXiv:2307.04840] [INSPIRE].

[16] R. Kumar et al., *Predictions from scoto-seesaw with A4 modular symmetry*, *Phys. Lett. B* **853** (2024) 138635 [arXiv:2310.02363] [INSPIRE].

[17] P. Van Dong et al., *Dark symmetry implication for right-handed neutrinos*, *Phys. Rev. D* **111** (2025) 035014 [arXiv:2407.02324] [INSPIRE].

[18] J. Schechter and J.W.F. Valle, *Neutrinoless Double beta Decay in $SU(2) \times U(1)$ Theories*, *Phys. Rev. D* **25** (1982) 2951 [INSPIRE].

[19] P.-H. Gu and U. Sarkar, *Radiative Neutrino Mass, Dark Matter and Leptogenesis*, *Phys. Rev. D* **77** (2008) 105031 [arXiv:0712.2933] [INSPIRE].

[20] Y. Farzan and E. Ma, *Dirac neutrino mass generation from dark matter*, *Phys. Rev. D* **86** (2012) 033007 [arXiv:1204.4890] [INSPIRE].

[21] E. Ma and O. Popov, *Pathways to Naturally Small Dirac Neutrino Masses*, *Phys. Lett. B* **764** (2017) 142 [arXiv:1609.02538] [INSPIRE].

[22] C. Bonilla et al., *Dark matter stability and Dirac neutrinos using only Standard Model symmetries*, *Phys. Rev. D* **101** (2020) 033011 [arXiv:1812.01599] [INSPIRE].

[23] A. Dasgupta, S.K. Kang and O. Popov, *Radiative Dirac neutrino mass, neutrinoless quadruple beta decay, and dark matter in B-L extension of the standard model*, *Phys. Rev. D* **100** (2019) 075030 [arXiv:1903.12558] [INSPIRE].

[24] S.-Y. Guo and Z.-L. Han, *Observable Signatures of Scotogenic Dirac Model*, *JHEP* **12** (2020) 062 [arXiv:2005.08287] [INSPIRE].

[25] S. Centelles Chuliá, R. Srivastava and S. Yadav, *Comprehensive phenomenology of the Dirac Scotogenic Model: Novel low-mass dark matter*, *JHEP* **04** (2025) 038 [arXiv:2409.18513] [INSPIRE].

[26] R. Kumar, N. Nath and R. Srivastava, *Cutting the scotogenic loop: adding flavor to dark matter*, *JHEP* **12** (2024) 036 [arXiv:2406.00188] [INSPIRE].

[27] D. Borah, P. Das, B. Karmakar and S. Mahapatra, *Discrete dark matter with light Dirac neutrinos*, *Phys. Rev. D* **111** (2025) 035032 [arXiv:2406.17861] [INSPIRE].

[28] R. Kumar, N. Nath and R. Srivastava, *Cutting the Scotogenic Loop: A_4 Flavor Symmetry to Z_2 Dark Symmetry*, *Springer Proc. Phys.* **304** (2024) 1183 [INSPIRE].

[29] E. Ma and G. Rajasekaran, *Softly broken A(4) symmetry for nearly degenerate neutrino masses*, *Phys. Rev. D* **64** (2001) 113012 [hep-ph/0106291] [INSPIRE].

[30] K.S. Babu, E. Ma and J.W.F. Valle, *Underlying A(4) symmetry for the neutrino mass matrix and the quark mixing matrix*, *Phys. Lett. B* **552** (2003) 207 [hep-ph/0206292] [INSPIRE].

[31] G. Altarelli and F. Feruglio, *Tri-bimaximal neutrino mixing, A(4) and the modular symmetry*, *Nucl. Phys. B* **741** (2006) 215 [hep-ph/0512103] [INSPIRE].

[32] M. Hirsch, S. Morisi, E. Peinado and J.W.F. Valle, *Discrete dark matter*, *Phys. Rev. D* **82** (2010) 116003 [arXiv:1007.0871] [INSPIRE].

[33] M.S. Boucenna et al., *Phenomenology of Dark Matter from A_4 Flavor Symmetry*, *JHEP* **05** (2011) 037 [arXiv:1101.2874] [INSPIRE].

[34] L.M.G. De La Vega, R. Ferro-Hernandez and E. Peinado, *Simple A_4 models for dark matter stability with texture zeros*, *Phys. Rev. D* **99** (2019) 055044 [arXiv:1811.10619] [INSPIRE].

[35] R.N. Mohapatra and J.W.F. Valle, *Neutrino Mass and Baryon Number Nonconservation in Superstring Models*, Phys. Rev. D **34** (1986) 1642 [INSPIRE].

[36] S. Centelles Chuliá, R. Srivastava and A. Vicente, *The inverse seesaw family: Dirac and Majorana*, JHEP **03** (2021) 248 [arXiv:2011.06609] [INSPIRE].

[37] E. Ma and R. Srivastava, *Dirac or inverse seesaw neutrino masses with $B-L$ gauge symmetry and S_3 flavor symmetry*, Phys. Lett. B **741** (2015) 217 [arXiv:1411.5042] [INSPIRE].

[38] E. Ma and R. Srivastava, *Dirac or inverse seesaw neutrino masses from gauged $B-L$ symmetry*, Mod. Phys. Lett. A **30** (2015) 1530020 [arXiv:1504.00111] [INSPIRE].

[39] E. Ma, N. Pollard, R. Srivastava and M. Zakeri, *Gauge $B-L$ Model with Residual Z_3 Symmetry*, Phys. Lett. B **750** (2015) 135 [arXiv:1507.03943] [INSPIRE].

[40] DESI collaboration, *DESI 2024 VI: cosmological constraints from the measurements of baryon acoustic oscillations*, JCAP **02** (2025) 021 [arXiv:2404.03002] [INSPIRE].

[41] KATRIN collaboration, *Direct neutrino-mass measurement with sub-electronvolt sensitivity*, Nature Phys. **18** (2022) 160 [arXiv:2105.08533] [INSPIRE].

[42] XENON collaboration, *First Dark Matter Search with Nuclear Recoils from the XENONnT Experiment*, Phys. Rev. Lett. **131** (2023) 041003 [arXiv:2303.14729] [INSPIRE].

[43] LZ collaboration, *First Dark Matter Search Results from the LUX-ZEPLIN (LZ) Experiment*, Phys. Rev. Lett. **131** (2023) 041002 [arXiv:2207.03764] [INSPIRE].

[44] ATLAS collaboration, *Search for invisible Higgs-boson decays in events with vector-boson fusion signatures using 139 fb^{-1} of proton-proton data recorded by the ATLAS experiment*, JHEP **08** (2022) 104 [arXiv:2202.07953] [INSPIRE].

[45] Q.-H. Cao, E. Ma and G. Rajasekaran, *Observing the Dark Scalar Doublet and its Impact on the Standard-Model Higgs Boson at Colliders*, Phys. Rev. D **76** (2007) 095011 [arXiv:0708.2939] [INSPIRE].

[46] M. Gustafsson, E. Lundstrom, L. Bergstrom and J. Edsjo, *Significant Gamma Lines from Inert Higgs Dark Matter*, Phys. Rev. Lett. **99** (2007) 041301 [astro-ph/0703512] [INSPIRE].

[47] A. Pierce and J. Thaler, *Natural Dark Matter from an Unnatural Higgs Boson and New Colored Particles at the TeV Scale*, JHEP **08** (2007) 026 [hep-ph/0703056] [INSPIRE].

[48] LZ collaboration, *Dark Matter Search Results from 4.2 Tonne-Years of Exposure of the LUX-ZEPLIN (LZ) Experiment*, Phys. Rev. Lett. **135** (2025) 011802 [arXiv:2410.17036] [INSPIRE].

[49] PandaX collaboration, *Dark Matter Search Results from 1.54 Tonne · Year Exposure of PandaX-4T*, Phys. Rev. Lett. **134** (2025) 011805 [arXiv:2408.00664] [INSPIRE].

[50] J. Billard, L. Strigari and E. Figueroa-Feliciano, *Implication of neutrino backgrounds on the reach of next generation dark matter direct detection experiments*, Phys. Rev. D **89** (2014) 023524 [arXiv:1307.5458] [INSPIRE].

[51] M.C. Gonzalez-Garcia and Y. Nir, *Neutrino Masses and Mixing: Evidence and Implications*, Rev. Mod. Phys. **75** (2003) 345 [hep-ph/0202058] [INSPIRE].

[52] MEG II collaboration, *A search for $\mu^+ \to e^+\gamma$ with the first dataset of the MEG II experiment*, Eur. Phys. J. C **84** (2024) 216 [*Erratum ibid.* **84** (2024) 1042] [arXiv:2310.12614] [INSPIRE].

[53] BaBar collaboration, *Searches for Lepton Flavor Violation in the Decays $\tau^\pm \to e^\pm\gamma$ and $\tau^\pm \to \mu^\pm\gamma$*, Phys. Rev. Lett. **104** (2010) 021802 [arXiv:0908.2381] [INSPIRE].

JHEP10(2025)088

[54] Belle collaboration, *Search for lepton-flavor-violating tau-lepton decays to $\ell\gamma$ at Belle*, *JHEP* **10** (2021) 019 [arXiv:2103.12994] [inSPIRE].

[55] A.M. Baldini et al., *MEG Upgrade Proposal*, arXiv:1301.7225 [inSPIRE].

[56] Belle-II collaboration, *Snowmass White Paper: Belle II physics reach and plans for the next decade and beyond*, arXiv:2207.06307 [inSPIRE].

[57] Particle Data Group collaboration, *Review of Particle Physics*, *PTEP* **2022** (2022) 083C01 [inSPIRE].

[58] F. Staub, *Exploring new models in all detail with SARAH*, *Adv. High Energy Phys.* **2015** (2015) 840780 [arXiv:1503.04200] [inSPIRE].

[59] W. Porod and F. Staub, *SPheno 3.1: Extensions including flavour, CP-phases and models beyond the MSSM*, *Comput. Phys. Commun.* **183** (2012) 2458 [arXiv:1104.1573] [inSPIRE].

[60] G. Bélanger, F. Boudjema, A. Pukhov and A. Semenov, *micrOMEGAs4.1: two dark matter candidates*, *Comput. Phys. Commun.* **192** (2015) 322 [arXiv:1407.6129] [inSPIRE].

[61] H. Ishimori et al., *Non-Abelian Discrete Symmetries in Particle Physics*, *Prog. Theor. Phys. Suppl.* **183** (2010) 1 [arXiv:1003.3552] [inSPIRE].